Geochemistry, Geophysics, Geosystems

RESEARCH ARTICLE
10.1029/2020GC009364

Reconstructing Magma Storage Depths for the 2018 Kīlauean Eruption From Melt Inclusion CO_2 Contents: The Importance of Vapor Bubbles

Penny E. Wieser[1], Hector Lamadrid[2], John Maclennan[1], Marie Edmonds[1], Simon Matthews[3], Kayla Iacovino[4], Frances E. Jenner[5], Cheryl Gansecki[6], Frank Trusdell[7], R.L. Lee[7], and Evgenia Ilyinskaya[8]

[1]Department of Earth Sciences, University of Cambridge, Cambridge, UK, [2]Geological Sciences, University of Missouri, Columbia, MO, USA, [3]Department of Earth and Planetary Sciences, Johns Hopkins University, Baltimore, MD, USA, [4]Jacobs, NASA Johnson Space Center, Houston, TX, USA, [5]School of Environment, Earth and Ecosystem Sciences, The Open University, Milton Keynes, UK, [6]Department of Geology, University of Hawai'i at Hilo, Hilo, HI, USA, [7]USGS Hawaiian Volcano Observatory, Hilo, HI, USA, [8]School of Earth and Environment, University of Leeds, Leeds, UK

Key Points:

- Petrological, gaseous and geophysical observations can be reconciled by a model where Fissure 8 was supplied from two summit storage reservoirs (~1–2- and 3–5-km depth)
- Extensive post-entrapment crystallization of melt inclusions within high-Fo olivines (Fo > 81.5) caused ~90% of the CO_2 to enter the vapor bubble
- Raman analyses of vapor bubbles combined with choice of a suitable H_2O-CO_2 solubility model is required to accurately determine magma storage depths

Supporting Information:

- Supporting Information S1

Correspondence to:
P. E. Wieser,
penny.wieser@gmail.com

Citation:
Wieser, P. E., Lamadrid, H., Maclennan, J., Edmonds, M., Matthews, S., Iacovino, K., et al. (2021). Reconstructing magma storage depths for the 2018 Kīlauean eruption from melt inclusion CO_2 contents: The importance of vapor bubbles. *Geochemistry, Geophysics, Geosystems*, *22*, e2020GC009364. https://doi.org/10.1029/2020GC009364

Received 7 AUG 2020
Accepted 2 DEC 2020

Abstract

The 2018 lower East Rift Zone (LERZ) eruption and the accompanying collapse of the summit caldera marked the most destructive episode of activity at Kīlauea Volcano in the last 200 years. The eruption was extremely well-monitored, with extensive real-time lava sampling as well as continuous geodetic data capturing the caldera collapse. This multiparameter data set provides an exceptional opportunity to determine the reservoir geometry and magma transport paths supplying Kīlauea's LERZ. The forsterite contents of olivine crystals, together with the degree of major element disequilibrium with carrier melts, indicates that two distinct crystal populations were erupted from Fissure 8 (termed high- and low-Fo). Melt inclusion entrapment pressures reveal that low-Fo olivines (close to equilibrium with their carrier melts) crystallized within the Halema'uma'u reservoir (~2-km depth), while many high-Fo olivines (>$Fo_{81.5}$; far from equilibrium with their carrier melts) crystallized within the South Caldera reservoir (~3–5-km depth). Melt inclusions in high-Fo olivines experienced extensive post-entrapment crystallization following their incorporation into cooler, more evolved melts. This favored the growth of a CO_2-rich vapor bubble, containing up to 99% of the total melt inclusion CO_2 budget (median = 93%). If this CO_2-rich bubble is not accounted for, entrapment depths are significantly underestimated. Conversely, reconstructions using equation of state methods rather than direct measurements of vapor bubbles overestimate entrapment depths. Overall, we show that direct measurements of melts and vapor bubbles by secondary-ion mass spectrometry and Raman spectroscopy, combined with a suitable H_2O-CO_2 solubility model, is a powerful tool to identify the magma storage reservoirs supplying volcanic eruptions.

Plain Language Summary

Pockets of frozen magma trapped within olivine crystals, termed "melt inclusions," can provide information about the depths at which magma is stored beneath the surface prior to a volcanic eruption. This is because the amount of CO_2 and H_2O that can be dissolved in a melt is dependent on the pressure, and therefore the depth. We examine melt inclusions from lava flows produced during the 2018 eruption of Kīlauea Volcano. Previous work, based on geophysics, has shown that magma is stored in two main reservoirs at Kīlauea, located at ~1–2- and ~3–5-km depth. However, because many melt inclusions host almost all of their CO_2 within a vapor bubble, which is rarely measured, previous petrological estimates of magma storage depths at Kīlauea do not align with the depths of the two reservoirs identified by geophysics. In this study, we measure the amount of CO_2 in the glass and the bubble using secondary-ion mass spectrometry and Raman spectroscopy, respectively. By adding these two measurements together, we can reconstruct the amount of CO_2 that was present when melt inclusions were trapped. Calculated depths align remarkably well with geophysical estimates, and demonstrate that the 2018 eruption was supplied by both magma storage reservoirs.

1. Introduction

The 2018 lower East Rift Zone (LERZ) eruption was the largest and most destructive in the last 200 years of activity at Kīlauea Volcano, Hawai'i (Neal et al., 2019), accompanied by the highest co-eruptive fluxes of SO_2 ever measured at Kīlauea (up to 200 kt a day; Kern et al., 2020; Whitty et al., 2020), and very high lava

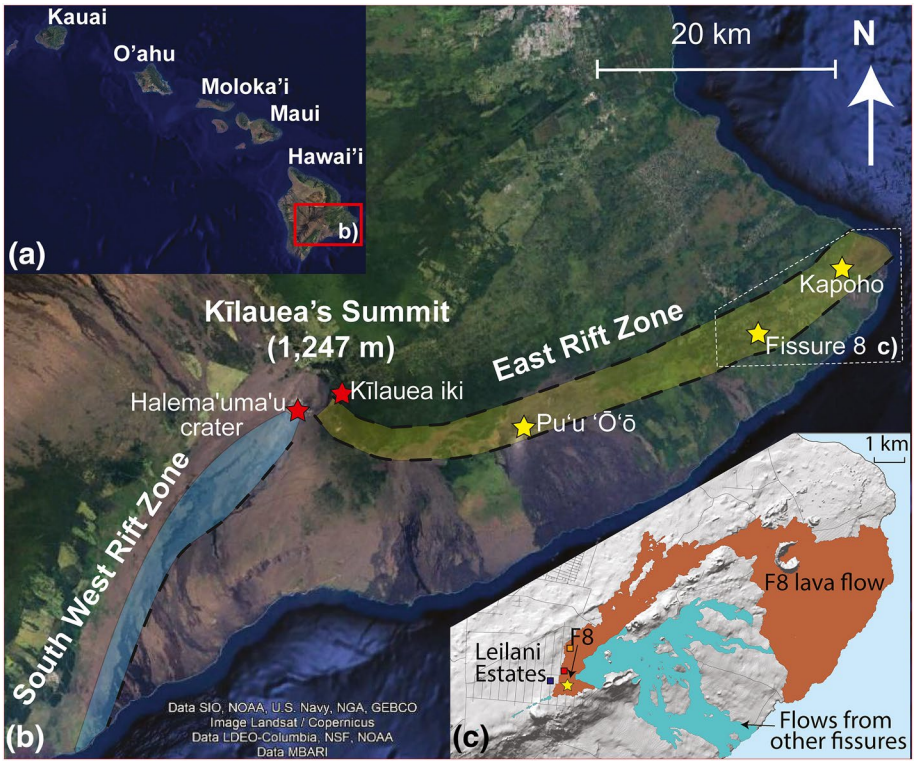

Figure 1. Map of Kīlauea Volcano (b), located on the southwest of the island of Hawai'i (a). Two prominent rift zones radiate from Kīlauea's summit caldera (b). The 2018 eruption occurred within the Leilani Estates subdivision on the lower East Rift Zone (LERZ; expanded region in c). The lava flows from Fissure 8 (marked with a yellow star) are colored deep orange, while flows from Fissures 1–7 and 9–24 are colored light blue. Sample locations are marked with squares (blue = May 2018, red = July 2018, orange = August 2018). Base maps for (a) and (b) are from Google Earth, and the map in (c) is adapted from Patrick, Dietterich et al. (2019).

effusion rates (100–300 m^3/s; Neal et al., 2019; Patrick, Dietterich et al., 2019). Before the onset of this new eruptive episode in May 2018, Kīlauea had been erupting near-continuously for 35 years on the middle East Rift Zone (ERZ) at Pu'u 'Ō'ō cone and surrounding vents, located approximately ~20 km east of Kīlauea's summit (1983–2018), and ~24-km uprift of the 2018 eruption site (Figure 1b). From 2008 to 2018, a persistently active lava lake was also present within Halema'uma'u (HMM) pit crater, located in the south west area of Kīlauea's summit caldera (Figure 1b).

The 2018 eruption was preceded by swarms of lower-crustal earthquakes at ~6–12-km depth beneath Kīlauea's summit area on March 7, April 11, and April 18, 2018 (Flinders et al., 2020). This inflation has been variably interpreted to result from a short-term increase in magma supply (Flinders et al., 2020), or a decrease in the output of magma along the ERZ to Pu'u 'Ō'ō, leading to magma backing up within the summit reservoir (Patrick et al., 2020). On March 13, 2018, inflation was recorded by tiltmeters located at Kīlauea's summit. Inflationary ground deformation also began at Pu'u 'Ō'ō, suggesting that excess magma was accumulating beneath this vent (Neal et al., 2019). The pressurization at these two locations continued throughout March and April, demonstrated by the rise of the lava pond at Pu'u 'Ō'ō, and overflows of the summit lava lake in mid-late April. On April 30, the crater floor at Pu'u 'Ō'ō collapsed, followed by an eastward migration of seismicity along the rift zone, consistent with the propagation of a dyke (Neal et al., 2019). A hazard notice released early in the morning of May 1 warned the residents of Lower Puna to be alert, as a large area along the ERZ east of Pu'u 'Ō'ō was at risk from a new outbreak of lava. Following the appearance of ground cracks in the Leilani Estates subdivision (Figure 1c) on May 2, lava reached the surface just before 5 p.m. on May 3 (Neal et al., 2019). Over the next few days, multiple fissures opened, preceded by gas emissions and ground cracking. In all, 24 fissures opened between May 3 and May 27, 2018.

Activity between May 3 and 9, classified as Early Phase 1 by Gansecki et al. (2019), was characterized by the eruption of spatter mounds and sluggish, slow-moving lava flows. This relatively evolved magma (mean SiO_2 = 51 wt% and MgO = 4 wt%; Gansecki et al., 2019; Lee et al., 2019) is thought to have formed by differentiation within LERZ storage reservoirs over decades to centuries (Neal et al., 2019). Throughout May, the compositions of erupted melts and crystals became increasingly primitive as summit-derived magma flushed out the LERZ storage reservoirs, with the exception of the involvement of an andesitic composition erupted in mid- to late-May (Gansecki et al., 2019). The eruption of hotter, less viscous lava led to the generation of fast-moving lava flows on May 18, which reached the coast 5 days later (Neal et al., 2019; Figure 1c). By May 28, activity had localized at Fissure 8 (F8), with the effusion of fast-flowing magma in a channelized flow (Patrick, Dietterich et al., 2019). Activity ended abruptly on August 4, by which time F8 had erupted ~1.5 km^3 of lava (Kauahikaua & Trusdell, 2020).

Despite the abundant geophysical and geochemical observations made during the LERZ eruption, the source of the magma erupted at F8 from late May–August 2018 has not yet been established. It is generally accepted that two main reservoirs are located beneath Kīlauea's summit. The shallower Halema'uma'u (HMM) reservoir is recognized as an inflation source located beneath the eastern rim of the HMM crater, and is thought to be centered at ~0.5–2-km depth (Anderson et al., 2019; Baker & Amelung, 2012; Cervelli & Miklius, 2003; Fiske & Kinoshita, 1969), while the deeper South Caldera (SC) reservoir manifests as an inflation source located beneath the southern portion of the caldera, at ~3–5-km depth (Baker & Amelung, 2012; Poland et al., 2015). The 2018 LERZ eruption was accompanied by large-scale subsidence of the caldera floor centered around the HMM crater (500 m in certain locations; Neal et al., 2019), which has been attributed to magma withdrawal from the underlying HMM reservoir to feed the effusion of lava from F8 (Anderson et al., 2019). However, recent estimates of the total SO_2 emissions requires the erupted volume to be approximately twice the modeled volume loss from the HMM reservoir, suggesting that a second magma source was involved (Kern et al., 2020).

In addition, the erupted crystal cargo from F8 contained some of the most forsteritic olivines (Fo_{88-89}) erupted at Kīlauea since 1974, which must have grown in melts with 13–14 wt% MgO (Gansecki et al., 2019). Some of these crystals also contain prominent kink bands (Gansecki et al., 2019), indicating that their crystal lattices have been deformed (Wieser, Edmonds et al., 2020). Previous work has suggested that highly forsteritic, deformed olivines are derived from the deeper, SC reservoir at 3–5-km depth (Helz et al., 2015, 2014; Wieser et al., 2019; Wieser, Edmonds et al., 2020), or Kīlauea's deep rift zones at 6–9-km depth (Clague & Denlinger, 1994; Vinet & Higgins, 2010). Alternatively, Lynn et al. (2017) suggest that highly forsteritic olivines from the Keanakāko'i Tephra may originate from deeper crustal storage reservoirs, perhaps located near the base of the volcanic pile at ~8–10-km depth.

Our study utilizes the strong pressure dependence of the solubility of CO_2 (and H_2O) in silicate melts to determine the pressures at which pockets of melt, termed melt inclusions, were trapped within olivine crystals. Through prior constraints on the density profile of the crust, entrapment pressures from F8 melt inclusions erupted in late-May, mid-July and early August 2018 can be converted into entrapment depths. In turn, these depths can be compared to geophysical estimates of the depths of the main magma storage regions at Kīlauea to determine the source(s) of magma erupted at F8.

2. Melt Inclusion Entrapment Pressures

2.1. The Importance of Vapor Bubbles

The solubility of pure CO_2 and H_2O in silicate melts is dependent on the pressure, the major element content of the melt, and the melt temperature. Assuming that a melt was saturated in a CO_2-H_2O fluid phase at the time of melt inclusion formation, the pressure at which a melt inclusion was trapped can be calculated by reconstructing its initial volatile and major element composition. In relatively water-poor systems like Kīlauea, where melts contain <1 wt% H_2O (Clague et al., 1995; Dixon et al., 1991; Sides, Edmonds, Maclennan, Houghton et al., 2014; Sides, Edmonds, Maclennan, Swanson et al., 2014; Tucker et al., 2019; Wallace & Anderson, 1998), the entrapment pressure is most sensitive to the CO_2 content of the melt, and its major element composition. Variations in melt H_2O content between 0 and 1 wt% have a relatively small effect on the entrapment pressure (except at very low CO_2 contents; see Supporting Information Figure S1; Newman & Lowenstern, 2002).

However, estimating the CO_2 content of a melt inclusion at the point of entrapment is not straightforward. The host crystal may experience a period of cooling after the melt inclusion was trapped, leading to the growth of olivine on the walls of the inclusion (termed post-entrapment crystallization [PEC]; Anderson & Brown, 1993; Danyushevsky et al., 2000; Roedder, 1984). The precipitation of denser olivine from the silicate melt, combined with the differential thermal contraction of the melt phase and the host olivine, causes the internal pressure of the melt inclusion to drop, driving the growth of a vapor bubble (Anderson, 1974; Anderson & Brown, 1993; Roedder, 1979). Combined with a reduction in the solubility of CO_2 associated with major element changes during PEC, these processes cause CO_2 to migrate from the melt phase into the bubble (Aster et al., 2016; Maclennan, 2017; Sides, Edmonds, Maclennan, Houghton et al., 2014; Steele-Macinnis et al., 2011). An additional phase of bubble growth is caused by the differential thermal contraction of the melt inclusion and the host olivine during syn-eruptive cooling from high magmatic temperatures (~1,150°C at F8; Gansecki et al., 2019; Helz & Thornber, 1987) to the glass transition temperature (~725°C; Ryan & Sammis, 1981).

Unfortunately, the vast majority of published volatile contents in melt inclusions globally, and at Kīlauea, only measured CO_2 in the glass phase, using techniques such as secondary-ion mass spectrometry (SIMS), or Fourier-transform infrared spectroscopy (FTIR; Bennett et al., 2019; Ruth et al., 2018; Sides, Edmonds, Maclennan, Houghton et al., 2014; Sides, Edmonds, Maclennan, Swanson et al., 2014). Given that recent work has shown that ~40%–90% of the total CO_2 budget of melt inclusions may be held within the vapor bubble (Hartley et al., 2014; Moore et al., 2015; Rasmussen et al., 2020; Wallace et al., 2015), entrapment pressures from studies neglecting vapor bubble carbon must be viewed as minimum estimates (Anderson & Brown, 1993; Ruth et al., 2018).

2.2. Reconstructing Vapor Bubble CO_2

Several approaches have been used to explore the contribution of vapor bubbles to the CO_2 budget of Hawaiian melt inclusions. Anderson and Brown (1993) theoretically reconstruct vapor bubble CO_2 by assuming that the melt and vapor bubble were in chemical equilibrium at high magmatic temperatures prior to syn-eruptive quenching. Specifically, they calculated melt inclusion internal pressures from glass CO_2 contents, and used these pressures to determine the molar volume of CO_2 in vapor bubbles using the CO_2 equation of state (EOS). They converted their molar volumes into CO_2 concentrations assuming that bubbles occupied 0.5 vol% of the melt inclusion prior to quenching, and added these values to measurements of glass CO_2 concentrations. Riker (2005) used a similar method to reconstruct bubble carbon for melt inclusions from the 1859 eruption of Mauna Loa. However, instead of using a fixed bubble volume, they account for the differential amounts of cooling and PEC experienced by erupted crystals, and calculate the bubble volumes prior to quench-induced expansion as a function of the drop in temperature (ΔT) between the melt inclusion at the point of entrapment and eruption (VB vol% $= 0.0162\ \Delta T - 0.0016$). More recently, Tucker et al. (2019) theoretically reconstructed bubble carbon contents for a large suite of melt inclusions from several Hawaiian volcanoes, including 167 from Kīlauea. However, instead of estimating the size of the vapor bubble prior to syn-eruptive quenching as in Anderson and Brown (1993) and Riker (2005), they used observed bubble volumes to convert CO_2 densities obtained from the EOS into bubble CO_2 concentrations. This approach is problematic because expansion of the bubble during syn-eruptive cooling and quenching continues until the glass transition temperature, while CO_2 diffusion through the melt into the bubble may effectively cease at a higher temperature. Thus, the final stages of bubble expansion will occur without concurrent CO_2 diffusion from the glass into the bubble, meaning that the EOS method will overpredict the amount of CO_2 in the bubble (Anderson & Brown, 1993; Maclennan, 2017; Rasmussen et al., 2020).

The total amount of CO_2 within melt inclusions can also be determined using experimental homogenization techniques, where crystals containing melt inclusions are heated to magmatic temperatures. This drives the dissolution of the olivine rim precipitated during PEC, which changes the chemistry and volume of the melt inclusion so that CO_2 held within the vapor bubble dissolves back into the melt. Following rapid quenching, the glass phase of these rehomogenized melt inclusions can be analyzed by SIMS or FTIR (Esposito et al., 2012; Rasmussen et al., 2020; Skirius et al., 1990; Tuohy et al., 2016; Wallace et al., 2015). However, experimental homogenization can lead to H_2O loss, excess dissolution of olivine on the walls of the melt inclusion, and loss of mineral and melt inclusion zoning, which degrades the overall utility of the

melt inclusion record (Rasmussen et al., 2020; Tuohy et al., 2016). In addition, it is not always possible to fully dissolve the original bubbles, and new bubbles containing CO_2 may nucleate upon quench (Rasmussen et al., 2020; Skirius et al., 1990; Tuohy et al., 2016; Wallace et al., 2015).

Most recently, the density of CO_2 in vapor bubbles has been measured directly using Raman spectroscopy (Aster et al., 2016; Esposito et al., 2011; Hartley et al., 2014; Moore et al., 2015, 2018; Steele-Macinnis et al., 2011; Taracsák et al., 2019). The Raman spectrum of CO_2 consists of two peaks nominally at 1,285 and 1,388 cm^{-1} at 1 bar (see Supporting Information Figure S2), resulting from the interaction of a symmetrical stretching mode and an active bending mode in the CO_2 molecule by a process known as Fermi resonance (Fermi, 1931; Lamadrid et al., 2017; Rosso & Bodnar, 1995). Hence, collectively, these peaks are referred to as the Fermi diad (FD), and the distance between the peak centers is the FD splitting (Δ). However, while it is well accepted that Δ correlates with CO_2 density (ρ_{CO_2}), there are a number of different parameterizations for this relationship in the literature (Kawakami et al., 2003; Lamadrid et al., 2017; Rosso & Bodnar, 1995; Wang et al., 2019; and references within). The diversity of published densimeters reflects different instrument hardware, as well as the choice of analytical conditions (Lamadrid et al., 2017). Thus, the approach used by a number of studies where a densimeter is chosen from the literature to convert measurements of Δ to ρ_{CO_2} on a different Raman instrument from the one used to calibrate the densimeter results in large systematic uncertainties in the absolute density of CO_2 (e.g., Hartley et al., 2014; Taracsák et al., 2019; Venugopal et al., 2020). For example, $\Delta = 102.8$ cm^{-1} yields $\rho_{CO_2} = 0.0281$ g/cm^3 using the densimeter of Wang et al. (2019), but $\rho_{CO_2} = 0.1397$ g/cm^3 using the densimeter of Kawakami et al. (2003). For a bubble volume of 5% (the 80th percentile of bubble volume proportions at Kīlauea from Tucker et al., 2019) and a melt density of 2.75 g/cm^3, these different densimeters predict a contribution of 538 ppm versus ~2,674 ppm CO_2 to the reconstructed total CO_2 budget of the melt inclusion. For a melt inclusion with $SiO_2 = 49$ wt%, and $H_2O = 0.5$ wt%, these CO_2 contents correspond to entrapment pressures of ~1.2 versus 4.8 kbar (at 1,200°C; Newman & Lowenstern, 2002), and entrapment depths of ~4 versus ~18 km, respectively, for a crustal density of 2,700 kg/m^3. Thus, the development of an instrument-specific calibration is essential to differentiate between lower and upper crustal storage at ocean island volcanoes, as well as fingerprint the involvement of different reservoirs identified by geophysical techniques.

An additional source of error affecting both Raman measurements and EOS methods arises during the conversion of ρ_{CO_2} into the equivalent amount of CO_2 in ppm held within the vapor bubble ($[CO_2]^{VB}$):

$$[CO_2]^{VB} = 10^6 \times \frac{\rho_{CO_2} V_{VB}}{\rho_{Melt} V_{Melt}} \quad (1)$$

where V_{VB} and V_{Melt} are the volume of the vapor bubble and the melt phase of the inclusion, respectively, and ρ_{Melt} is the density of the silicate melt calculated here using DensityX (Iacovino & Till, 2019). Total CO_2 contents are obtained by summing the equivalent amount of CO_2 in the vapor bubble with the concentration of CO_2 measured in the melt phase ($[CO_2]^{Melt}$) by SIMS or FTIR:

$$[CO_2]^{Tot} = [CO_2]^{VB} + [CO_2]^{Melt} \quad (2)$$

The volumes of the vapor bubble and melt inclusion are typically determined from two-dimensional (2D) transmitted light images, estimating the length of the third, unmeasurable dimension from the major and minor axes of the plan view of the inclusion. Tucker et al. (2019) simulate this process by randomly intersecting ellipses and show that the smallest errors are achieved by calculating the third dimension as the arithmetic mean of the two measured axes. However, this approach is still associated with a 1σ error of −47 to +37% (Tucker et al., 2019). Although important, we note that this random error is entirely overwhelmed by the systematic error of up to a factor of four in literature data sets which have arbitrarily chosen a literature densimeter.

To mitigate the systematic error associated with Raman calibration, we determine the relationship between Δ and ρ_{CO_2} for the specific instrument and acquisition conditions used in this study through the analysis of synthetic fluid melt inclusions with known CO_2 densities. Analysis of both the melt phase (using SIMS) and the vapor bubble (using a calibrated Raman system) yields the first extensive data set that allows critical evaluation of the contribution of vapor bubbles to the total CO_2 budget of specific melt inclusions at

Kīlauea. Combined with a rigorous examination of the suitability of different CO_2-H_2O solubility models, these measurements place accurate constraints on entrapment depths of olivine-hosted melt inclusions from the 2018 LERZ eruption. This data set, combined with quantitative models of bubble growth, also allows assessment of the relative importance of PEC and syn-eruptive quenching on the partitioning of CO_2 between the melt and vapor phase. In turn, this allows the accuracy of EOS methods as an alternative to direct measurements of ρ_{CO_2} using Raman spectroscopy to be evaluated.

3. Materials and Methods

3.1. Sample Details, Preparation and Analytical Methods

We examine three samples erupted at F8 (square symbols; Figure 1c):

1. May 2018 (erupted May 30, 2018; USGS code KE62–3293; blue symbols), comprising vesicular reticulite and scoria which landed in a bucket placed near the F8 vent (19°27.7486'N, 154°54.8636'W).
2. July 2018 (erupted mid-July 2018; red symbols), from the selvages of a naturally quenched, and highly vesicular proximal overflow from the F8 channel (<50 m from the vent; 19°27.879'N, 154°54.645'W).
3. August 2018 (erupted August 1; USGS code KE62–3321F; orange symbols), which was sampled directly from the F8 channel using a metal rod and chain, and rapidly quenched in water. Direct lava sampling took place on a stable channel levee (19°28.31508'N, 154°54.51426'W), ~700 m downstream of the position of the July 2018 overflow.

Samples were jaw crushed and sieved into three size fractions (250–840, 840–1,000, and >1,000 μm). Olivines were picked under a binocular microscope, and individually mounted in CrystalBond™ on glass slides. Care was taken to prepare melt inclusions hosted within olivine crystals from all three size fractions. Melt inclusions were exposed by grinding with 250–3,000 grade wet and dry paper, allowing embayments to be avoided, and melt inclusions containing vapor bubbles to be identified. Melt inclusions without vapor bubbles were ground down with progressively finer wet and dry paper until the center of the inclusion was exposed. Melt inclusions containing vapor bubbles were ground down to just above the top of the melt inclusion of interest (to avoid intersecting the bubble, and releasing the trapped CO_2). A photo was taken of the melt inclusion and vapor bubble using a transmitted light microscope to allow estimation of melt inclusion and bubble volumes. For larger melt inclusions, two images were acquired: one where the bubble was in focus, and one where the melt inclusion outline was in focus. The outline of the bubble and melt inclusion were traced using ImageJ (Schneider et al., 2012), and a best fit ellipse was fitted to each. Volumes were calculated by assuming that the third (nonmeasurable dimension) was equal to the arithmetic mean of the two measured dimensions (Tucker et al., 2019). Several melt inclusions contained large spinel crystals that were likely coentrapped. The volume of these spinels (assuming a cuboid shape, with the third dimension also equal to the arithmetic mean of the visible dimensions) was subtracted from the volume of the melt inclusion.

Following optical measurements, crystals were ground down until the vapor bubble was within ~30 μm of the surface. Depending on the optical quality after fine grinding (using 2,000–7,000 grade wet and dry paper), melt inclusions were variably polished using 9 μm diamond pastes prior to Raman analysis. Raman spectra of vapor bubbles were collected using a confocal LabRAM 300 (Horiba Jobin Yvon) Raman spectrometer in the Department of Earth Sciences at the University of Cambridge. Fermi diads were fitted with Gaussian peaks after subtracting a polynomial fit to the background (see Supporting Information Figure S4). The relationship between Δ and ρ_{CO_2} for the specific Raman acquisition condition used in this study was determined by analyzing 16 synthetic CO_2-H_2O fluid inclusions with a range of densities (~0.04, ~0.08, and ~0.14 g/cm^3) hosted in quartz, as well as three Kīlauean melt inclusion vapor bubbles. The densities of all 19 of these primary standards were measured using a JY Horiba LabRam HR in the Fluids Research Laboratory at Virginia Tech Raman, which has been specifically calibrated for low CO_2 densities using a high-pressure optical cell (Lamadrid et al., 2017). A linear regression through repeated measurements of these standards on the Cambridge Raman yielded the following relationship with 95% confidence intervals on the regression (see Supporting Information Figure S3):

$$\rho_{CO_2}(g\ /\ cm^3) = 0.3217 \pm 0.026\ \Delta\ (\mathrm{cm}^{-1}) - 32.995 \pm 2.7 \quad (3)$$

Further analytical details are presented in the Supporting Information (Text S1). Following Raman analyses, individual crystals were ground down to expose the center of each melt inclusion to maximize the available analyzable area. The bubble was exposed in approximately half of bubble-bearing inclusions. Following sonication to remove polishing residue, exposed bubble walls were examined on the FEI Quanta 650FEG SEM at the University of Cambridge in low vacuum mode prior to the application of any coatings. Crystals were then mounted in epoxy in groups of 20–40, and polished with progressively finer diamond pastes (9, 6, 3, 1, 0.25 μm).

Following the application of a gold coat, the concentrations of H_2O and CO_2 (as well as MgO and SiO_2 for normalization) in melt inclusions and coerupted matrix glasses were determined using the Cameca IMS-7f GEO at the NERC Ion Microprobe Facility, University of Edinburgh. SIMS analysis was performed prior to electron probe microanalyzer (EPMA) analysis to avoid volatile migration under the electron beam, and to avoid contamination of measured carbon concentrations by a carbon coat. Epoxy stubs were placed in the sample chamber at vacuum for a minimum of 6 h before analysis to allow them to outgas. A wide variety of standards were analyzed to create calibration curves for H_2O and CO_2 (N71, M10, 519-4-1, M5, M40, M36, M21, M47, M36; see Supporting Information S5; Hauri, 2002; Shishkina et al., 2010). Additional information regarding calibration, background and drift corrections are provided in the Supporting Information (Text S2).

Following SIMS analyses, the Au coat was removed by polishing on a 0.25-μm diamond polishing pad, and a carbon coat was applied for EPMA analyses. Spot analyses of melt inclusions, matrix glasses and host olivines were obtained using a Cameca SX100 EPMA in the Department of Earth Sciences, University of Cambridge following the two-condition analytical set up described in Wieser et al. (2019). Spectrometer configurations, count times, calibration materials, and estimates of precision and accuracy calculated from repeated analyses of secondary standards (San Carlos Olivine, VG2 and A99; Jarosewich, 2002) are presented in the Supporting Information (Text S3, Tables S2–S4).

Melt inclusion compositions were corrected for the effects of PEC using the Olivine MI tool in Petrolog3 (Danyushevsky & Plechov, 2011). This tool requires the user to specify the initial FeO_T and the host Fo content of each inclusion. FeO_T was set at 11.33 wt% for melt inclusions hosted in olivines with forsterite contents ([Fo = $Mg^{2+}/(Mg^{2+}+Fe^{2+})$ atomic]) >79 mol% based on the liquid line of descent at Kīlauea, and for consistency with previous studies (Sides, Edmonds, Maclennan, Swanson et al., 2014; Wieser et al., 2019). For olivine crystals with Fo < 79 mol%, the initial FeO content was estimated from the relationship between the equilibrium olivine forsterite content and melt FeO_T contents in a fractional crystallization model computed in MELTS for MATLAB (Supporting Information Figure S5; Antoshechkina & Ghiorso, 2018; Gualda et al., 2012).

4. Results

F8 melt inclusions are hosted in olivine crystals with a wide range of core compositions ($Fo_{77\text{-}89}$; Figure 2a). Core compositions in all three samples show a peak at ~$Fo_{88\text{-}89}$ (Figures 2b–2d), which lies significantly above the equilibrium field calculated from the Mg# of coerupted matrix glasses [Mg# = $Mg^{2+}/(Mg^{2+} + Fe^{2+})$, atomic], even considering a wide range of experimentally determined values for $K^{ol-melt}_{D\mathrm{Fe}^{2+}-\mathrm{Mg}^{2+}}$ (black lines, Figure 2a; 0.270–0.352; Matzen et al., 2011; Roeder & Emslie, 1970). Fourteen melt inclusions from May 2018, but only six melt inclusions from July 2018 and one from Aug 2018 are hosted in olivines which lie within the equilibrium field. F8 olivines have some of the highest Fo contents ever reported at Kīlauea (Figures 2a–2d vs. Figures 2e and 2f; Sides, Edmonds, Maclennan, Swanson et al., 2014; Wieser et al., 2019), but relatively low carrier melt Mg#s (51–57 mol%; assuming $Fe^{3+}/Fe_T = 0.15$). In turn, this juxtaposition produces some of the most extreme degrees of olivine-carrier melt Fe-Mg disequilibrium seen at Kīlauea (Figure 2a). Crystals with high forsterite cores show strong normal zoning, while crystals with core compositions plotting closer to the equilibrium field on Figure 2a are not visibly zoned in rapid EDS acquisitions (see Supporting Information Figures S7–S9).

The majority of F8 melt inclusions exhibit lower measured FeO_T contents than coerupted matrix glasses and the composition of Kīlauean melt inclusions from the literature (gray dots; Sides, Edmonds, Maclennan, Houghton et al., 2014; Sides, Edmonds, Maclennan, Swanson et al., 2014; Tucker et al., 2019; Wieser

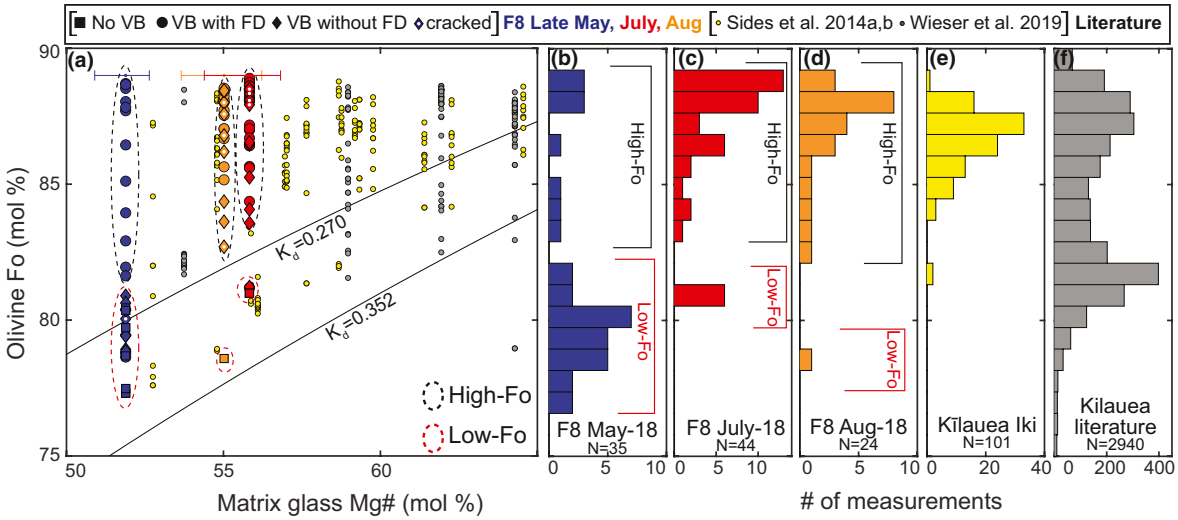

Figure 2. Olivine populations and olivine-melt relationships at F8 compared to literature data. (a) Core olivine forsterite content versus matrix glass Mg# for $Fe^{3+}/Fe_T = 0.15$ (Helz et al., 2017; Moussallam et al., 2016). Olivines lying between the black lines ($K_D = 0.270–0.352$) are in equilibrium with their carrier melts considering the range of experimentally determined Fe-Mg partition coefficients (Matzen et al., 2011; Roeder & Emslie, 1970). F8 olivines have some of the highest Fo contents observed at Kīlauea, yet are hosted in carrier liquids with some of the lowest Mg#s. Literature data from Wieser et al. (2019), Sides, Edmonds, Maclennan, Houghton et al. (2014), and Sides, Edmonds, Maclennan, Swanson et al. (2014). (b)–(d) Histograms of olivine Fo contents from this study, (e) Kīlauea Iki (Sides, Edmonds, Maclennan, Houghton et al., 2014; Sides, Edmonds, Maclennan, Swanson et al., 2014), and (f) the compilation of literature analyses presented in Wieser et al. (2019) combined with new measurements from Tucker et al. (2019). The strong bimodality in F8 forsterite contents, along with the degree of olivine-melt disequilibrium was used to subdivide melt inclusions into those hosted within high-Fo olivines (black-dotted outline) and low-Fo olivines (red-dotted outline). Olivines are further subdivided into those hosting a melt inclusion without a vapor bubble (no VB), with a vapor bubble which produces a Fermi diad (VB with FD), those with a vapor bubble that does not produce a Fermi diad (VB without FD). Melt inclusions which are cracked, and have a vapor bubble without a FD, are indicated with a white dot.

et al., 2019). Melt inclusion MgO contents are more similar to those of coerupted matrix glasses (Figure 3a). Following a correction for the effects of PEC, F8 melt inclusions have MgO contents between 6.4 and 13.7 wt%, and FeO_T contents between 11.3 and 12 wt% (Figure 3a, Supporting Information Figure S5). Despite the high degree of Mg# disequilibrium between olivine crystals and their carrier melts (Figure 2a), measured melt inclusion Mg#s (uncorrected for the effects of PEC) mostly lie within, or close to the equilibrium field calculated from the core compositions of their host olivines (Figure 3b). The distance from the equilibrium field degree is largest in the July 2018 sample, but still smaller than the vast majority of melt inclusions data from other Kīlauean eruptions, particularly those hosted in olivines with higher Fo contents (Figure 3b). Melt inclusions hosted in olivine crystals which have the highest degree of disequilibrium with their carrier melts (calculated by subtracting the equilibrium Fo content of the coerupted matrix glass from the Fo content of each olivine) have experienced the most PEC (Figure 3c) and have the lowest measured FeO_T contents (Figure 3d).

To encapsulate the variable degrees of olivine-melt disequilibrium, and to aid comparisons between different crystal populations, we subdivide F8 olivines into two groups. The first group contains olivines which lie within, or close to the equilibrium field calculated from the Mg# of the coerupted matrix glass (Figure 2a). For the May 2018 sample, the division was placed at $Fo_{81.5}$, based on the near continuous distribution of olivines from slightly above to within the equilibrium field (which can easily be generated by slight cooling between crystallization and eruption), and the slight gap between these olivines and those with higher Fo contents (Figure 2b). The second group contains olivines which lie outside the equilibrium field. For brevity, these groups are referred to as low-Fo and high-Fo olivines, although this classification evaluates the forsterite content of the olivine relative to the Mg# of the coerupted matrix glass, rather than the absolute Fo content (see Figure 3c). A similar classification for the eruptions on Figure 2 with higher glass Mg#s would place the boundary between groups at higher Fo contents (e.g., the Fo_{84} division used by Wieser et al., 2019).

All high-Fo melt inclusions contain a vapor bubble (Figure 3c), 73% ($N = 53$) of which produce a FD during Raman analysis. Vapor bubbles which do not produce a FD may contain no CO_2, or CO_2 densities below

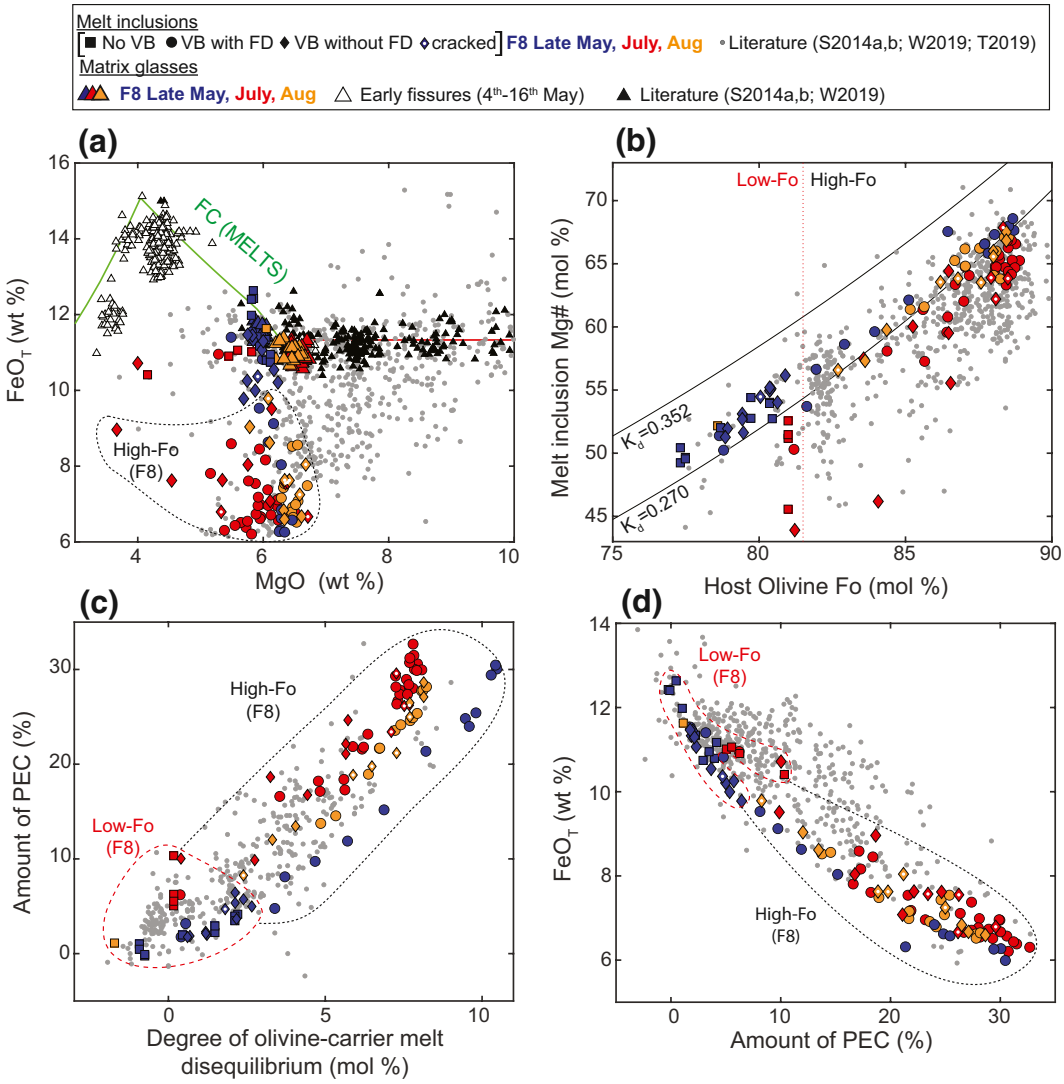

Figure 3. Measured major element systematics for F8 melt inclusions (uncorrected for the effects of PEC). (a) High-Fo F8 melt inclusions have significantly lower FeO_T contents than liquid line of descent defined by Kīlauean matrix glasses from (this study, Sides, Edmonds, Maclennan, Houghton et al., 2014; Wieser et al., 2019), and a MELTS for MATLAB (Antoshechkina & Ghiorso, 2018; Gualda et al., 2012) fractionation path following the onset of clinopyroxene and plagioclase fractionation (green line) which recreates glass compositions erupted from earlier, more evolved fissures during the 2018 eruption (4–5 wt% MgO, white triangles). Despite highly variable FeO_T contents, the MgO contents of melt inclusions mostly align with those of their coerupted matrix glasses. (b) In contrast to the prominent disequilibrium between high-Fo olivine compositions and coerupted matrix glasses (Figure 1a), melt inclusion Mg#s uncorrected for the effects of PEC (for $Fe^{3+}/Fe_T = 0.15$) plot close to the equilibrium field with their host olivines (particularly melt inclusions from the May 2018 and Aug 2018 samples). Melt inclusions from previous Kīlauean eruptions (Sides, Edmonds, Maclennan, Houghton et al., 2014; Sides, Edmonds, Maclennan, Swanson et al., 2014; Tucker et al., 2019; Wieser et al., 2019, gray dots) lie much further below the equilibrium field. (c) The amount of PEC (calculated in Petrolog3; Danyushevsky & Plechov, 2011) is strongly correlated with the degree of ol-melt disequilibrium, calculated by subtracting the equilibrium olivine composition of the coerupted matrix glass (for $K_D = 0.3$) from the measured Fo content. (d) The FeO_T contents of F8 melt inclusions also shows a strong negative correlation with the amount of PEC, extending to lower values than the vast majority of literature data. PEC, post-entrapment crystallization.

the detection limit of Raman spectroscopy. While the detection limit will depend on the exact depth of the bubble below the surface, as well as the transparency of the host crystal, the distribution of densities in vapor bubbles which produced a FD indicates that the detection limit lies between 0 and 0.02 g/cm^3 (light green bar in Figure 4c). Nine of the bubbles without a FD are hosted within cracked melt inclusions, which

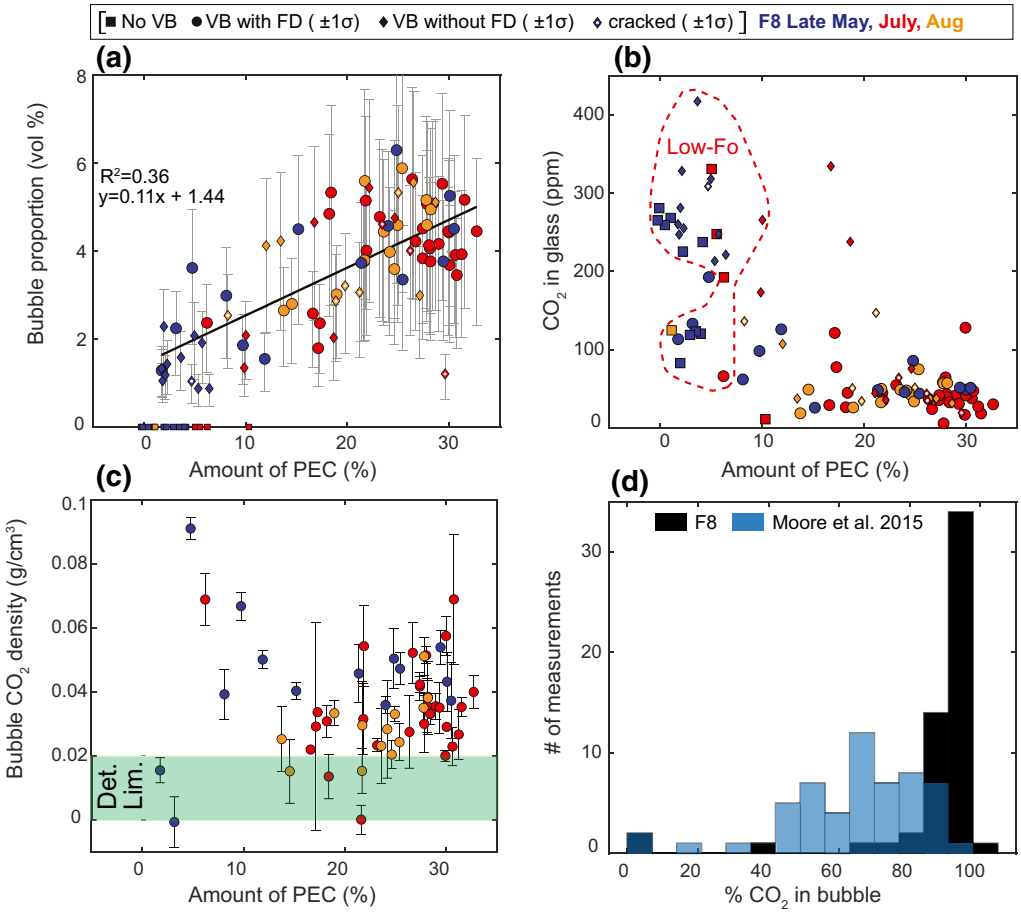

Figure 4. Vapor bubble and melt inclusion CO_2 systematics. (a) There is a positive correlation between the volume proportion of the vapor bubble (VB) and the amount of post-entrapment crystallization (PEC). Only melt inclusions which have experienced <10% PEC are bubble-free. Error bars show the 1σ errors associated with estimating bubble volume proportions from 2D images (−45% and +37%; Tucker et al., 2019). (b) With increasing amounts of PEC, the amount of CO_2 within the glass phase of the melt inclusion declines. The highest glass CO_2 contents are observed in melt inclusions with no vapor bubbles (squares), and melt inclusions with bubbles that did not produce a FD (diamonds). In contrast, the vast majority of melt inclusions with low glass CO_2 contents have vapor bubbles which produced a FD (circles), or vapor bubbles without a FD that were hosted within cracked melt inclusions (diamonds with white dots). (c) There is no correlation between the CO_2 density in vapor bubble measured using Raman spectroscopy and the amount of PEC. Error bars show the ±1σ deviation of three repeated measurements of each vapor bubble. The green bar shows our estimate of the detection limit (Det. Lim.) of Raman analyses based on the distribution of measured bubble densities. (d) The black histogram shows the proportion of CO_2 held within the vapor bubble for F8 melt inclusions that produced a FD (mean = 87%, median = 93%). Estimates by Moore et al. (2015) for Kīlauean melt inclusions from the 1959 and 1960 eruptions are also shown.

may have resulted in CO_2 loss from the bubble (diamonds with white dots; Figures 3 and 4, see Supporting Information Figure S10, Aster et al., 2016). In contrast, only 50% ($N = 15$) of low-Fo melt inclusions contain a vapor bubble, and only 20% ($N = 3$) of these produce a FD (Figure 3c). Only one of the bubbles without a FD is hosted within a cracked melt inclusion.

Bubble-bearing melt inclusions show a correlation between the volume % of the bubble and the amount of PEC, despite the large random errors associated with measuring bubble volume proportions from 2D images (gray error bars; Figure 4a). There is a substantial drop in glass CO_2 contents with increasing PEC, and melt inclusions containing vapor bubbles with a FD show significantly lower glass CO_2 contents than bubble-free melt inclusions (Figure 4b, $p = 10^{-7}$; Kolmogorov-Smirnov [KS] test). There is no obvious correlation between the CO_2 density in vapor bubbles and the amount of PEC (Figure 4c, $R^2 = 10^{-5}$), the CO_2 density and the glass CO_2 content ($R^2 = 0.1$) or the CO_2 density and the volume of the bubble ($R^2 = 0.0004$).

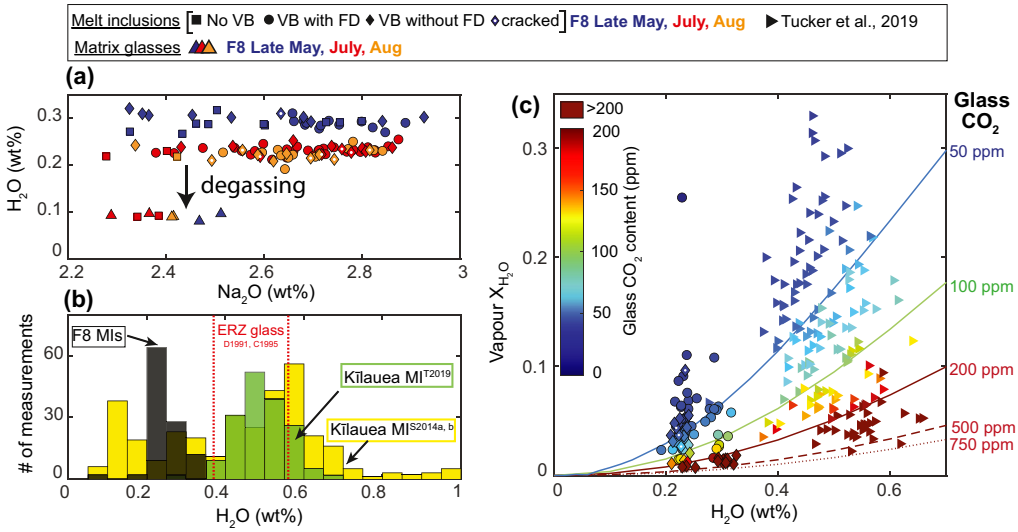

Figure 5. H_2O systematics of F8 melt inclusions relative to literature data from Kīlauea. (a) F8 melt inclusion H_2O contents are remarkably constant within each sample, despite substantial variations in Na_2O. This indicates that melt inclusion H_2O contents were reset by diffusive re-equilibration with their carrier liquid. The precision of SIMS measurements (±1.5%) is smaller than the symbol size, so error bars are not shown. (b) F8 melt inclusions have lower H_2O contents than the majority of Kīlauean melt inclusions measured by Sides, Edmonds, Maclennan, Swanson et al. (2014); Sides, Edmonds, Maclennan, Houghton et al. (2014) (yellow histogram) and almost all of the melt inclusions measured by Tucker et al. (2019). H_2O contents from submarine ERZ glasses with 7–16 wt% MgO from Dixon et al. (1991) and Clague et al. (1995) are shown with red dashed lines. (c) Relationship between the molar fraction of H_2O in the vapor phase (X_{H_2O}) and the melt H_2O content for five different melt CO_2 contents (50, 100, 200, 500, and 750 ppm; using VolatileCalc-Basalt; Newman & Lowenstern, 2002). X_{H_2O} ratios for the coexisting vapor in equilibrium with the measured concentration of CO_2 and H_2O in the melt phase of the bubble-bearing inclusions from this study and Tucker et al. (2019) (triangles) are overlain, with symbols colored by the CO_2 content of the glass phase. The relatively low H_2O contents of F8 melt inclusions mean that X_{H_2O} is generally <0.1. However, a number of inclusions from Tucker et al. (2019) with glass CO_2 contents <100 ppm have much higher X_{H_2O} ratios. This causes the CO_2 densities predicted using the EOS method to fall below the trend line defined by F8 melt inclusions on Figure 8a. EOS, equation of state; ERZ, East Rift Zone; SIMS, secondary-ion mass spectrometry.

The median and mean proportion of the total melt inclusion CO_2 budget hosted within the bubble is 93% and 87%, respectively (black histogram; Figure 4d). This exceeds the proportions calculated by Moore et al. (2015) for melt inclusions from the 1959 and 1960 eruptions of Kīlauea (median = 67%, mean = 65%; blue histogram). This discrepancy reflects the fact that Moore et al. (2015) did not measure the CO_2 content of the glass in each melt inclusion, so they calculated proportions assuming a glass CO_2 content of 300 ppm (the maximum measured in the same suite of samples by Tuohy et al., 2016). Our new data shows the importance of measuring CO_2 in the glass and bubble of a specific melt inclusion; while bubble-free melt inclusions have CO_2 contents up to 417 ppm in the glass phase, those with vapor bubbles producing a FD have median CO_2 contents of only 45 ppm (mean = 54 ppm; Figure 4b). In contrast to the highly variable CO_2 contents in melt inclusion glasses, H_2O contents are remarkably constant within a given eruption, despite significant variation in the contents of incompatible elements such as Na_2O and K_2O (Figure 5a). Excluding two degassed melt inclusions (~0.09 wt% H_2O), F8 melt inclusions have between 0.19 and 0.33 wt% H_2O, which is lower than most of the Kīlauean melt inclusions measured by Sides, Edmonds, Maclennan, Houghton et al. (2014); Sides, Edmonds, Maclennan, Swanson et al. (2014) and almost all of those measured by Tucker et al. (2019) (Figure 5b).

5. Discussion

5.1. Mineral-Melt Disequilibrium Drives the Growth of a CO_2-Rich Bubble

The prominent Mg# disequilibrium between the core compositions of high-Fo olivines from F8 and their carrier melts has been observed in a number of historic eruptions at Kīlauea (Figure 2; Sides, Edmonds,

Maclennan, Houghton et al., 2014; Sides, Edmonds, Maclennan, Swanson et al., 2014; Tuohy et al., 2016; Wieser et al., 2019). Based on major and trace element disequilibrium between melt inclusions and their carrier melts (e.g., Nb/Y ratios), as well as microstructures consistent with deformation of the crystal lattice (also observed in some high-Fo olivines from F8 by Gansecki et al., 2019), Wieser, Edmonds et al. (2020) and Wieser et al. (2019) suggested that highly forsteritic olivines are scavenged from long-lived plastically deforming mush piles at the base of the SC reservoir, and incorporated into cooler, lower Mg# carrier melts with different trace element signatures just prior to eruption. These studies also suggest that olivines with lower forsterite contents exhibiting small amounts of olivine-melt disequilibrium (similar to the low-Fo olivines in this study), no lattice distortions, and a high degree of trace element equilibrium may have crystallized from their carrier melts as true phenocrysts. The distinct populations of high- and low-Fo olivines examined here may have similar origins.

Kīlauean melts with greater than ~6.8 wt% MgO are saturated in only olivine and minor chrome-spinel (Wright & Fiske, 1971), so show a strong correlation between temperature and the MgO content of the melt (Helz & Thornber, 1987). The remarkably constant FeO contents of high MgO Kīlauean melts (Figure 3a) means that glass Mg# is strongly correlated with MgO, and therefore temperature. As glass Mg# is closely related to the olivine forsterite content through the Fe-Mg olivine-liquid exchange coefficient, equilibrium olivine forsterite contents are also strongly correlated with temperature. Thus, the difference in Mg# between the measured olivine core composition, and the equilibrium olivine forsterite content calculated from the composition of coerupted matrix glasses (termed the degree of olivine-melt disequilibrium) is proportional to the amount of cooling experienced by the inclusion prior to syn-eruptive quenching (Wieser et al., 2019). The close relationship between the amount of cooling experienced by an inclusion, and the amount of PEC (Danyushevsky et al., 2000) accounts for the excellent correlation between the degree of olivine-melt disequilibrium and the amount of PEC (Figure 3c).

F8 melt inclusions are hosted in some of the most forsteritic olivines erupted at Kīlauea, yet were erupted in carrier melts with some of the lowest Mg#s (Figure 2a). Consequently, they have experienced some of the largest amounts of cooling following entrapment, and, by extension, some of the largest amounts of PEC ever reported at Kīlauea (up to ~33%; Figure 3c), see also Lerner (2020) and Lerner et al. (2020). These PEC extents are also significantly larger than those reported from other volcanic systems; olivine-hosted melt inclusions from Holuhraun (Iceland), Piton de la Fournaise (Réunion), and Erebus (Antarctica) have experienced ~5%, <12%, and 0%–4.2% PEC, respectively (Collins et al., 2012; Hartley et al., 2015; Moussallam et al., 2014). The small amounts of cooling (and therefore PEC) experienced by low-Fo olivines, which are close to equilibrium with their carrier melts, likely occurred during fractionation between the formation and eruption of these crystals (Figure 3c). However, progressive fractionation and cooling of a batch of melt cannot account for the peak at ~$Fo_{88\text{-}89}$ in F8 samples (Maaløe et al., 1988; Wieser et al., 2019), nor the paucity of olivines with Fo contents in equilibrium with the coerupted matrix glasses (particularly in the July and August samples; Figure 2a). Based on the similarities between the high-Fo olivines from F8 and previous studies (large amounts of olivine-melt disequilibrium, presence of lattice distortions; Gansecki et al., 2019), we appeal to the process proposed by Wieser et al. (2019), where cooling is not a gradual process during progressive differentiation of a given magma batch (Maaløe et al., 1988), but occurs over short timescales, when high-Fo olivine crystals residing in hot mush piles are mixed into significantly cooler, lower Mg# melts (Sides, Edmonds, Maclennan, Houghton et al., 2014; Wieser et al., 2019), see also Shea et al. (2019).

Melt inclusion MgO and FeO_T contents are strongly affected by the crystallization of olivine on the walls of the melt inclusion (PEC), and subsequent diffusive re-equilibration. Based on the strong coupling between MgO content and temperature in olivine-saturated liquids (Helz & Thornber, 1987), thermal equilibration of a hot olivine crystal with a cooler carrier melt drives the crystallization of a zoned olivine rim from the melt inclusion, causing the MgO content of the melt inclusion to drop to match that of the carrier melt (Figure 3a). This zoned olivine rim begins to re-equilibrate with the host crystal, and, in turn, the melt inclusion re-equilibrates with the changing rim composition (Danyushevsky et al., 2000). The melt inclusion loses FeO by diffusion to achieve Mg# equilibration with the host olivine following the large initial drop in MgO during cooling. As the MgO content of the melt inclusion is a function of the temperature, FeO diffusion is countered by MgO diffusion in the opposite direction, which is sequestered by further PEC of olivine on the wall of the melt inclusion.

This FeO-loss process accounts for the negative correlation between melt inclusion FeO_T contents and the amount of PEC (Figure 3d). For a given amount of PEC, F8 melt inclusions have lower FeO_T contents and display a smaller degree of Mg# disequilibrium with their olivine host than the vast majority of literature data (Figures 3b and 3d). It is important to note that methods calculating the amount of PEC based on the degree of Mg# disequilibrium between the melt inclusion and the host crystal (e.g., Neave et al., 2017; Tucker et al., 2019) will significantly underestimate the true amount of PEC in melt inclusions where extensive FeO-loss has occurred compared to the Petrolog3 method used here where the user specifies an initial FeO_T content. For example, the May 2018 melt inclusions with Fo > 85 have lost sufficient quantities of FeO by diffusive re-equilibration such that their Mg#s are in equilibrium with the composition of the host olivine. Thus, methods based on Mg# comparisons would indicate that these melt inclusions have experienced very minor amounts of PEC. However, their FeO contents lie ~4 wt% below the composition of coerupted matrix glasses, indicating that their compositions have been heavily altered by the PEC process (Figure 3a).

The higher degrees of diffusive FeO-loss for a given amount of PEC for F8 melt inclusions compared to literature data (Figure 3d) indicates that there was a longer time lag between the entrainment of crystals into cooler melts and their eventual eruption. Danyushevsky et al. (2002) quantitatively model Fe-Mg re-equilibration to estimate this time lag: their Figure 4c shows that a melt inclusion with a ~50 μm radius that has experienced ΔT = 100°C–150°C and undergone FeO loss at T = 1,150°C–1,200°C achieves 98% equilibrium in ~2 years. These extents of cooling and temperatures of re-equilibration are representative of F8 inclusions. However, Danyushevsky et al. (2002) assume isotropic diffusion of Fe through the host olivine crystal with $D_{Fe, Mg}$ = ~3–6 × 10^{-17} m^2/s at 1,150°C–1,200°C. In reality, FeO loss will be dominated by diffusion along the fast c-direction in olivine ($D_{Fe, Mg}$ = ~1–4 × 10^{-16} m^2/s for Fo_{80-89}, T = 1,150°C–1,200°C, and QFM to QFM + 0.3; Barth et al., 2019; Chakraborty, 2010). Thus, complete re-equilibration could be achieved almost an order of magnitude faster, in a matter of months. Considering the substantial uncertainties in this method associated with the fact the model of Danyushevsky et al. (2002) does not account for diffusional anisotropy, and the fact the degree of re-equilibration is very sensitive to the choice of K_D (Figure 3b), the FeO_T systematics of melt inclusions within high-Fo olivines erupted on May 28 (~70%–100% re-equilibration) indicate that entrainment into cooler carrier melts occurred approximately a month to a year prior to eruption.

5.2. Diffusive H_2O-Loss

Given that H_2O in melt inclusions diffusively re-equilibrates over hours to days (Gaetani et al., 2012; Hartley et al., 2015; Le Voyer et al., 2014), the timescales inferred from Fe-Mg re-equilibration are more than sufficient for H_2O contents within F8 melt inclusions to be fully reset to the H_2O content of the melt which carried them to the site of the eruption. This re-equilibration accounts for the remarkably uniform H_2O contents of F8 melt inclusions in each sample, despite substantial variation in the concentration of other incompatible elements (e.g., Na_2O; Figure 5a). The approximately constant H_2O contents in melt inclusions from each sample indicates that F8 carrier melts erupted in late-May had H_2O contents of 0.29 wt%, while those erupted in July and August had slightly lower H_2O contents (~0.22–0.23 wt%). These carrier melts are relatively H_2O-poor compared to the composition of previously erupted Kīlauean melts (inferred from published melt inclusion and submarine glass data; Figure 5). The presence of more H_2O-poor carrier melts in 2018 likely results from the extensive mixing of magmas which had partially degassed their H_2O at the summit lava lake with undegassed melts within the plumbing system between 2008 and 2018 (see also Lerner, 2020), similar to the mechanism proposed for Puna Ridge magmas by Dixon et al. (1991).

5.3. PEC and Melt-Vapor CO_2 Partitioning

It is well-recognized that extensive PEC drives the growth of a CO_2-rich vapor bubble (Aster et al., 2016; Maclennan, 2017; Sides, Edmonds, Maclennan, Houghton et al., 2014; Sides, Edmonds, Maclennan, Swanson et al., 2014; Steele-Macinnis et al., 2011). Thus, studies measuring only the CO_2 in the melt phase using SIMS or FTIR will yield spuriously low entrapment depths for melt inclusions which have undergone extensive PEC (e.g., Sides, Edmonds, Maclennan, Houghton et al., 2014). Our concurrent measurements of CO_2 in the melt and bubble phase of a large number of melt inclusions which have experienced a wide range of PEC amounts (Figures 3c and 3d) provides a unique opportunity to interrogate the various processes causing CO_2 to partition into the vapor bubble.

To investigate the effects of compositional changes in the melt inclusion associated with PEC, we use the CO_2 solubility model of Shishkina et al. (2014):

$$\ln\left[CO_2\right] = 1.15\ln\left(P\right) + 6.71\Pi^* - 1.345 \quad (4)$$

where $[CO_2]$ is the concentration of CO_2 in ppm, and P is the pressure in MPa. The Π* term accounts for the compositional dependence on CO_2 solubility, expressed in terms of the cation fractions of seven major element species:

$$\Pi^* = \frac{Ca^{2+} + 0.8K^{+} + 0.7Na^{+} + 0.4Mg^{2+} + 0.4Fe^{2+}}{Si^{4+} + Al^{3+}} \quad (5)$$

We calculate the change in Π* during PEC, ΔΠ*, by subtracting the Π* value of the PEC-corrected major element composition of each melt inclusion from the Π* value of the measured composition. ΔΠ* becomes progressively more negative with increasing amounts of PEC, showing that CO_2 becomes progressively less soluble (red dots; Figure 6b, see also Maclennan, 2017). Changes in Π* are dominated by a decrease in X_{Mg}, and increase in X_{Si} and X_{Al} resulting from the crystallization of olivine on the walls of the inclusion. These changes are partially counteracted by an increase in X_{Ca} (as Ca is incompatible in olivine). To quantify the magnitude of this drop in Π* in terms of CO_2 partitioning between the melt and bubble, we consider the eight melt inclusions which have experienced >30% PEC (all of which contain bubbles which produce a FD). The mean Π* value of the measured compositions of these melt inclusions is 0.33, while the mean Π* of their PEC-corrected compositions is 0.39 ($\Delta\Pi^* = -0.068$). For $P = 0.76$ kbar, which is the average entrapment pressure for the PEC-corrected compositions of these melt inclusions calculated using Equation 4, CO_2 solubility drops by ~192 ppm. As melts at Kīlauea are CO_2 saturated at crustal storage depths (Gerlach et al., 2002), this extra CO_2 will partition into the vapor bubble.

However, the mean amount of CO_2 sequestered within the vapor bubbles of these eight melt inclusions is 657 ± 231 ppm (calculated using Equation 1). This reflects three additional processes which enhance CO_2 partitioning into the bubble during PEC. First, the crystallization of olivine, which contains negligible quantities of CO_2, drives up the total concentration of the CO_2 in the remaining melt by a factor of one plus the amount of PEC (1.3–1.33× for these eight melt inclusions). As mentioned above, because Kīlauea melt inclusions are CO_2 saturated (Gerlach et al., 2002), the excess partitions into the bubble (mean 145 ppm, up to 230 ppm CO_2). Second, the preferential contraction of the melt phase relative to the olivine during thermal re-equilibration leads to a reduction in the volume of the melt phase. This volume reduction is enhanced by the third process; the crystallization of denser olivine on the rim of the melt inclusion. A drop in the internal pressure of the melt inclusion causes the CO_2 solubility to decrease further, driving more CO_2 into the vapor bubble (Equation 5). Evidence for these volume changes is provided by the correlation between the amount of PEC and the volume of the vapor bubble (Figure 4a), as well as the observation that all melt inclusions without a vapor bubble have experienced <10% PEC (Figure 4a), while all melt inclusions that have experienced >10% PEC have a vapor bubble.

Overall, changes in melt chemistry, the incompatible behavior of CO_2, and a drop in the internal pressure of the melt inclusion accounts for the rapid decrease in glass CO_2 contents with increasing PEC (Figure 4b). Our concurrent measurements of glass and bubble CO_2 provide the first opportunity to see through these convoluting effects of PEC to robustly determine total CO_2 contents, and therefore entrapment depths of Kīlauean melt inclusions. To account for the uncertainty regarding the amount of CO_2 held within bubbles that did not produce a FD (diamond symbols), particularly those hosted within cracked olivines (diamond symbols with white dot), we only calculate total CO_2 contents and entrapment depths for melt inclusions which had no bubble, or a bubble that produced a FD. These total CO_2 contents were corrected for the incompatible behavior of CO_2 during PEC to determine the total CO_2 content at the point of melt inclusion entrapment.

Total PEC-corrected CO_2 contents in melt inclusions hosted within high-Fo olivines are offset to significantly higher values compared to those hosted within low-Fo olivines (Figure 7a), indicating that these two olivine populations crystallized at distinct depths within Kīlauea's plumbing system. It is also interesting to compare our total CO_2 contents to previously published data on Kīlauean melt inclusions. Although these

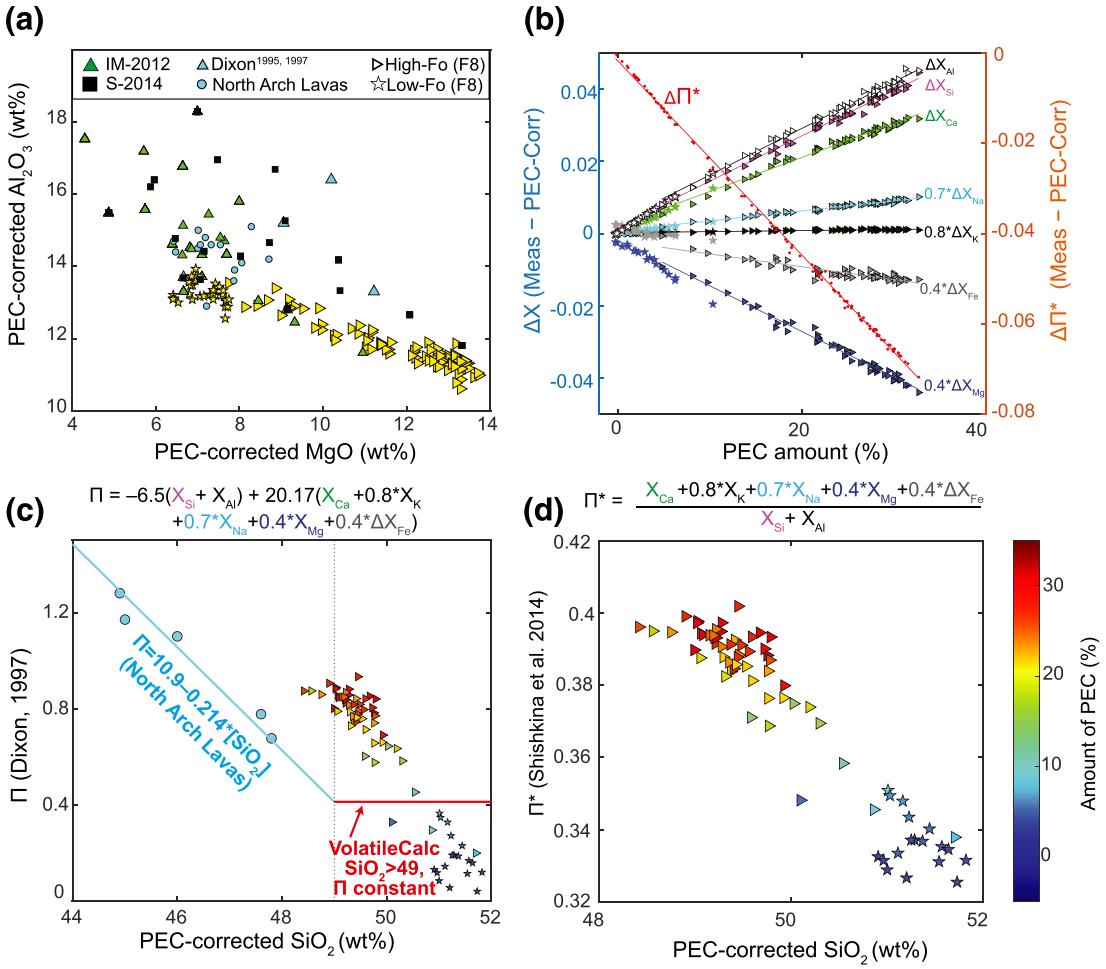

Figure 6. Evaluating the compositional sensitivity of CO_2 solubility. (a) Comparison of the MgO versus Al_2O_3 systematics of PEC-corrected F8 inclusions to the glass compositions used to calibrate each solubility model. The North Arch lavas which define the simplified Π versus SiO_2 relationship presented in Dixon (1997) and implemented in VolatileCalc-Basalt (Newman & Lowenstern, 2002) are also shown (blue circles). The MagmaSat data set (Ghiorso & Gualda, 2015) includes the experiments in the calibration data sets of Shishkina et al. (2014), Iacono-Marziano et al. (2012), and Dixon et al. (1995) (so is not shown, as it would cover all these symbols). (b) ΔX (triangle and star symbols) and ΔΠ* (red dots Shishkina et al., 2014) for F8 melt inclusions plotted against the amount of PEC. ΔX and ΔΠ* were calculated by subtracting the values of X and Π* for PEC-corrected melt inclusions from the values of X and Π* for measured compositions. For example, inclusion LL8_156 has experienced 33% PEC, and has a PEC-corrected MgO content of 13.5 wt% and a measured MgO content of 5.4 wt%. Thus, ΔX_{Mg} is strongly negative. (c) The compositional parameter Π of Dixon (1997) calculated for PEC-corrected F8 melt inclusion compositions varies substantially with SiO_2, following an offset trend to that defined by North Arch Glasses (Dixon et al., 1997, blue dots and linear regression). VolatileCalc-Basalt effectively treats all melt inclusions with >49 wt% SiO_2 as if Π is constant (red line). (d) The compositional parameter Π* from Shishkina et al. (2014), and therefore the solubility of CO_2, is significantly higher for high-Fo melt inclusions (which have the highest PEC-corrected MgO, and lowest SiO_2 and Al_2O_3 contents). The color of the symbols for F8 melt inclusions in (c) and (d) represents the amount of PEC. PEC, post-entrapment crystallization.

studies investigate products from different eruptions, the apparent stability in the geometry of Kīlauea's plumbing system since at least the 1950s (Eaton & Murata, 1960; Helz et al., 2014; Poland et al., 2015) means such comparisons are still useful (and particularly relevant for studies of the 1959–1960 eruptive period, where activity at the summit was followed by a large LERZ eruption; e.g., Moore et al., 2015; Sides, Edmonds, Maclennan, Houghton et al., 2014; Sides, Edmonds, Maclennan, Swanson et al., 2014; Tuohy et al., 2016). Unsurprisingly, given our finding that ~90% of CO_2 is held within the vapor bubble (Figure 4d), CO_2 contents in F8 melt inclusions are significantly higher than measurements of just the glass phase by Sides, Edmonds, Maclennan, Swanson et al. (2014) and Sides, Edmonds, Maclennan, Houghton et al. (2014) (Figure 7c). F8 melt inclusions are also offset to higher CO_2 contents than experimentally rehomogenized melt inclusions (Tuohy et al., 2016; Figure 7d). Tuohy et al. (2016) note similar offsets between their measurements and Raman reconstructions of bubble CO_2 by Moore et al. (2015) in the same sample set. They suggest that their analyses may have been biased toward melt inclusions with smaller bubbles that

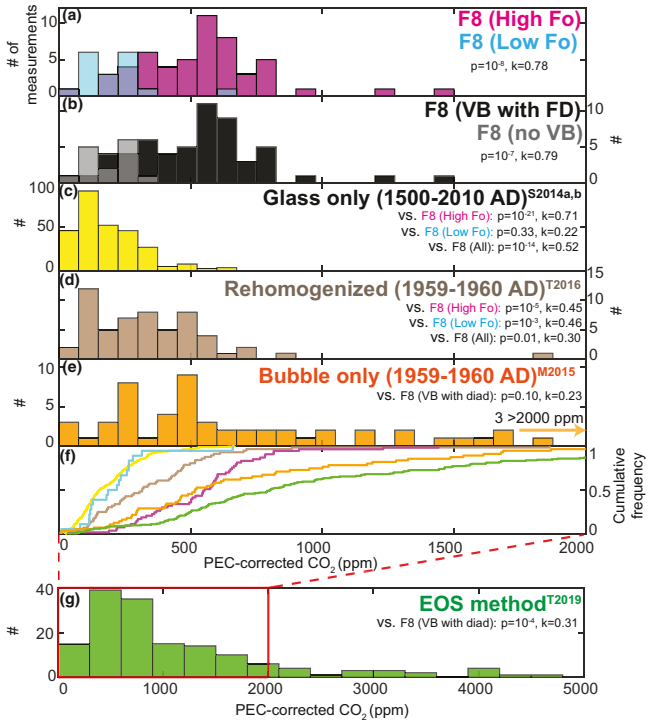

Figure 7. Histograms of melt inclusion CO_2 contents from this study and the literature (all corrected for the effects of PEC). (a) Total CO_2 contents (bubble + glass) for high- and low-Fo melt inclusions are statistically distinguishable at $p = 0.05$ using the Kolmogorov-Smirnov (KS) test (p value and test statistic k shown on the figure). (b) Similarly, melt inclusions which contain a vapor bubble (VB) with a FD have significantly higher total CO_2 contents than bubble-free melt inclusions. (c) Melt inclusion CO_2 contents from a suite of eruptions at Kīlauea between 1500 and 2008 AD where only the glass phase was measured (Sides, Edmonds, Maclennan, Houghton et al., 2014; Sides, Edmonds, Maclennan, Swanson et al., 2014). (d) CO_2 contents of experimentally homogenized melt inclusions from the 1959 Kīlauea Iki and 1960 Kapoho eruptions (Tuohy et al., 2016). (e) Bubble CO_2 contents from Moore et al. (2015) in the same suite of samples as in (d). For consistency, these bubble CO_2 contents were corrected for PEC using the average amount of PEC reported by Tuohy et al. (2016) (13%). (f) Cumulative distribution plots for these data sets. (g) Total PEC-corrected melt inclusion CO_2 contents from Tucker et al. (2019) where the contribution from bubble CO_2 was estimated using the EOS method (excluding inclusions with bubble volumes >8% that the authors suggest were coentrapped). Thirty-five melt inclusions have $CO_2 > 1{,}500$ ppm. Note the change in x-axis scale from plots (a)–(f). For literature data, all melt inclusions are shown, as Fo contents were not reported by Moore et al. (2015), and matrix glass Mg#s were not reported in Tucker et al. (2019), so it was not possible to classify data based on the degree of olivine-melt disequilibrium as for F8 samples. EOS, equation of state; FD, Fermi diad; PEC, post-entrapment crystallization.

fully disappear upon heating, lower pressure inclusions that do not fracture during heating, and larger inclusions that can be analyzed by FTIR.

Interestingly, our distribution of total CO_2 contents for melt inclusions which possessed bubbles are indistinguishable using the KS test ($p = 0.1$) from the CO_2 contribution of just the vapor bubbles in melt inclusions from the 1959 and 1960 eruptions of Kīlauea (Moore et al., 2015; Figure 7e). This demonstrates that in olivine populations which have experienced extensive PEC, measurements of glass CO_2 contents are of subordinate importance to measurements of bubble CO_2. Furthermore, the contribution of CO_2 from the melt phase for the majority of high-Fo melt inclusions from F8 is entirely overwhelmed by the errors on the amount of CO_2 in the bubble associated with estimating bubble volume proportions from 2D images. However, it is worth noting that only measuring CO_2 in vapor bubble would have failed to identify the population of low-Fo olivines which host almost all of their CO_2 within the glass phase. Thus, we suggest that future studies use a small number of SIMS or FTIR analyses of melt inclusions, combined with EPMA analyses of host crystals and melt inclusions, to determine the relationship between glass and bubble CO_2 contents and the amount of PEC in different subpopulations of melt inclusions. If the vast majority of CO_2 in a given population is held in the vapor bubble, a limited analytical budget would be better spent accurately measuring bubble volumes (using MicroCT or 3D Raman mapping; Pamukcu et al., 2013; Venugopal et al., 2020) to combine with Raman measurements of CO_2 density in the rest of the sample set, instead of precisely quantifying the insignificant amount of CO_2 held within the glass phase using SIMS or FTIR.

Importantly, we also observe that the distribution of total CO_2 contents in bubble-bearing melt inclusions is significantly higher than bubble-free melt inclusions (Figure 7b). This result invalidates the approach of preferentially targeting bubble-free melt inclusions to avoid having to account for CO_2 within the vapor bubbles (e.g., Esposito et al., 2011; Helo et al., 2011) in systems where erupted crystals have experienced extensive PEC prior to eruption. Crucially, analysis of only bubble-free melt inclusions by SIMS or FTIR, or analyses of just vapor bubbles using Raman, would have failed to identify that crystals are supplied from two distinct storage regions within Kīlauea's plumbing system.

5.4. Analytical versus Theoretical Constructions of Vapor Bubble CO_2

In contrast to the good agreement between our estimates of total CO_2 contents from combined SIMS and Raman measurements from F8 and the bubble-only measurements of Moore et al. (2015), the total CO_2 contents estimated by Tucker et al. (2019) for a range of Kīlauean eruptions using the EOS method are displaced to significantly higher values (Figure 7g). To assess the cause of this discrepancy, we follow the EOS method they describe to calculate CO_2 bubble densities for F8 melt inclusions to compare to our Raman measurements. The simplification of the Dixon (1997) solubility model implemented in the excel workbook VolatileCalc (hereafter VolatileCalc-Basalt; Newman & Lowenstern, 2002) was used to calculate the internal pressure of the melt inclusion based on the measured SiO_2, CO_2, and H_2O contents of the glass phase. The pure CO_2 EOS of Span and Wagner (1996) implemented in Python3 through CoolProp (Bell et al., 2014) was used to calculate the CO_2 density at this internal pressure and 725°C, which was the presumed glass transition temperature of Tucker et al. (2019) based on Ryan and Sammis (1981). The Duan

and Zhang (2006) EOS utilized by Tucker et al. (2019) yields identical densities to the fourth decimal place (see Supporting Information Figure S11). The more significant source of error involves the choice of the glass transition temperature. This is fixed at 725°C in Tucker et al. (2019) and 825°C in Moore et al. (2015) (dashed and solid magenta line; Figure 8a) for simplicity, but in reality, varies as a function of cooling rate and melt viscosity (and, by extension, melt composition; Giordano et al., 2005; Maclennan, 2017). The average glass transition temperatures predicted by the bubble-growth python code MIMiC (which uses the model of Giordano et al., 2005; Rasmussen et al., 2020) for bubble-bearing F8 melt inclusions for cooling rates of 10°C/s is 680°C (dotted magenta line; Figure 8a). Following Tucker et al. (2019), we multiply the density obtained from the pure-CO_2 EOS by the mole fraction of CO_2 (X_{CO_2}) in the vapor phase determined in VolatileCalc (Newman & Lowenstern, 2002). This correction neglects the nonideal mixing of H_2O and CO_2 at magmatic temperatures compared to the use of a mixed H_2O-CO_2 EOS (e.g., Moore et al., 2015) but is probably a reasonable approximation for relatively dry systems such as Kīlauea (Figures 5a and 5b).

The dominant control of the glass CO_2 content on the internal pressure of the inclusion in relatively anhydrous melts, and the positive relationship between the internal pressure and ρ_{CO_2} from the EOS evaluated at a constant temperature, means that predicted ρ_{CO_2} values increase with increasing glass CO_2 contents (Figure 8a). Predicted CO_2 densities from Tucker et al. (2019) plot on or below the quadratic fit through the EOS predictions for F8 melt inclusions at 725°C (magenta solid line), because of the higher values of X_{H_2O} (and thus lower X_{CO_2}) for a number of melt inclusions which possess high glass H_2O, but low glass CO_2 contents (Figure 5c). However, unlike the predictions from the EOS method, there is no correlation between ρ_{CO_2} measured using Raman spectroscopy and glass CO_2 contents ($R^2 = 0.11$). Interestingly, all melt inclusions with >200 ppm CO_2 in the glass have vapor bubbles which did not produce a FD (diamond symbols; Figure 8a), indicating that their CO_2 densities were below the detection limit of Raman spectroscopy (~0–0.02 g/cm^3; green bar in Figure 4c). It seems implausible that these bubbles could possess the high CO_2 densities predicted by the EOS (ρ_{CO_2} >0.2 g/cm^3) and fail to produce a FD. Furthermore, melt inclusions with ρ_{CO_2} > 0.2 g/cm^3 will consist of an outer shell of liquid CO_2, and an inner sphere of vapor CO_2 at room temperature (~21°C–22°C). For ρ_{CO_2} = 0.4 g/cm^3, this liquid phase will comprise 26% of the radius of the bubble, and the motion of the inner sphere of vapor by Brownian motion would be readily observable under an optical microscope. Yet, we observe no two-phase bubbles, and there are no reports of two-phase bubbles in the Kīlauean literature.

The fundamental tenet of the EOS method used by Tucker et al. (2019) is that CO_2 continues to partition between the vapor bubble and the melt until the bubble stops growing at the glass transition temperature. However, during syn-eruptive quenching, the strong temperature dependence of CO_2 diffusivity means that the diffusion of CO_2 from the melt into the bubble may cease before the bubble reaches its final volume (Anderson & Brown, 1993). Continued bubble growth without concurrent diffusion causes the density of CO_2 within the bubble to drop below that predicted from the EOS (Aster et al., 2016; Maclennan, 2017; Moore et al., 2015). Nonequilibrium bubble expansion has been proposed to account for the presence of vapor bubbles in Icelandic melt inclusions with CO_2 concentrations below the detection limit of Raman spectroscopy (Neave et al., 2014).

The discrepancy between EOS predictions and Raman measurements ($\Delta\ \rho_{CO_2}$) increases linearly with glass CO_2 content ($R^2 = 0.78$; shown as an absolute discrepancy, Figure 8b) and decreases with the amount of PEC (shown as a factor, Figure 8c). Melt inclusions containing bubbles without a FD lie within the confidence interval of the regression through bubbles which produced a FD if the Raman detection limit (0.02 g/cm^3) is subtracted from CO_2 densities calculated from the EOS (Figure 8b). To investigate these correlations, we assess the relative contribution of bubble growth at high magmatic temperatures during PEC and ascent (where CO_2 diffusion and bubble growth are coupled) compared to bubble growth during quench (where CO_2 diffusion is temperature-limited, and therefore decoupled from the mechanical expansion of the bubble).

We model melt inclusions from the point of entrapment to the glass transition temperature using the model of Maclennan (2017; Figure 9). Quench rates of 10°C/s were used based on video footage of the sampling and quenching of the August 2018 sample; ~40 s elapsed between the sample being pulled from the channel (~1,150°C) and becoming brittle at the glass transition temperature (~725°C; Tucker et al., 2019). At these

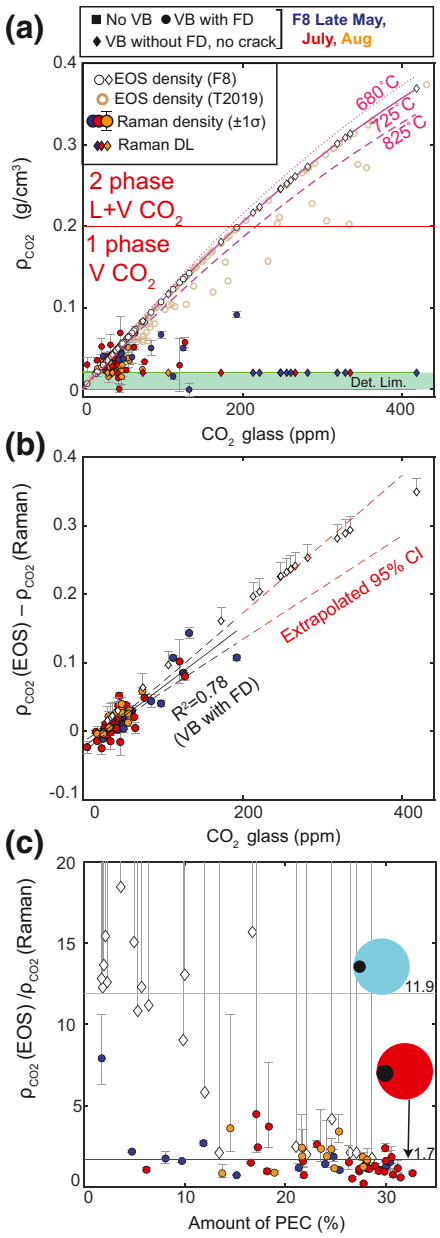

Figure 8. Comparisons of bubble CO_2 densities calculated using the EOS with those measured by Raman spectroscopy. (a) Calculated ρ_{CO_2} correlates strongly with glass CO_2. Bubbles within F8 melt inclusions are shown as white circles and diamonds (FD and no FD), bubbles within melt inclusions from Tucker et al. (2019) are shown as beige hollow circles. Magenta lines shows quadratic fits through calculated bubble densities for F8 melt inclusions for the EOS evaluated at 680°C, 725°C, and 825°C. A number of inclusions with low inclusion CO_2 contents and high H_2O contents from Tucker et al. (2019) lie below this line, because of their higher X_{H_2O} values (Figure 5c). Measured ρ_{CO_2} in this study are shown as colored circles, with error bars showing the 1σ of repeated acquisitions of each bubble. Colored diamonds (no FD, not cracked) are plotted at 0.02 g/cm^3 (the presumed detection limit of Raman spectroscopy; see Figure 4c). (b) The absolute discrepancy between predicted and measured ρ_{CO_2}, $\Delta\ \rho_{CO_2}$, correlates strongly with glass CO_2 content. The 95% confidence interval on a linear regression for measured bubble densities is shown with red dotted lines. Bubbles which did not produce a FD lie within error of the extrapolated confidence interval (assuming $\rho_{CO_2} = 0.02$ g/cm^3). (c) To allow comparison with bubble growth models in Figure 9, the discrepancy between EOS methods and Raman measurements are shown as a factor (as above, VB without a FD assumed to contain 0.02 g/cm^3). The proportion of the total bubble volume grown during quench for the high- and low-Fo models shown in Figure 9 are shown with red and cyan lines, respectively. Error bars in (b) and (c) for VB with FD show the 1σ uncertainty of repeated Raman measurements, and those for VB without FD are calculated for DL between 0 and 0.02 g/cm^3 (hence they extend to infinity in c). EOS, equation of state; FD, Fermi diad.

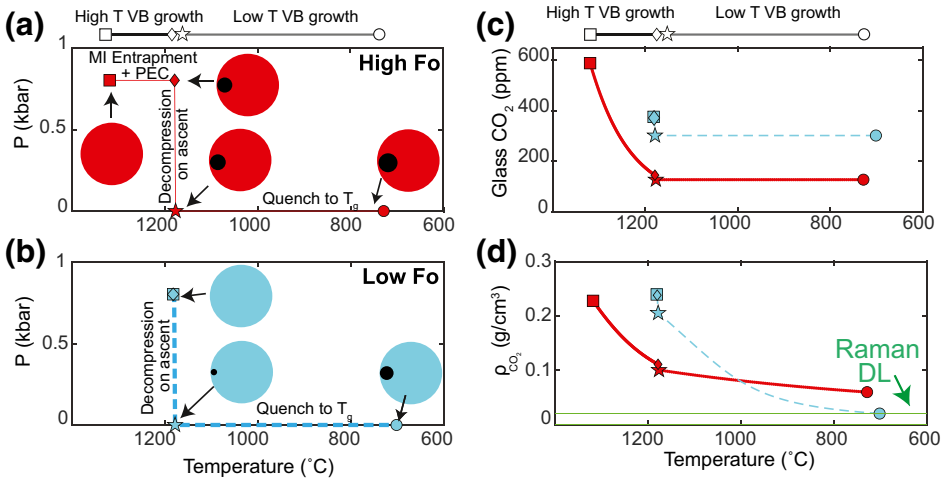

Figure 9. Model of CO_2 partitioning between the melt and bubble for PT scenarios representative of inclusions hosted within high- and low-Fo olivines (red and blue colors, respectively). (a) The red melt inclusion experiences considerable cooling ($\Delta T = 150$°C) and post-entrapment crystallization at high temperatures and pressures (square to diamond symbol), driving the growth of a vapor bubble. This high temperature phase of bubble growth is accompanied by CO_2 diffusion from the melt to the bubble, causing the glass CO_2 content to drop substantially (c). This inclusion then ascends to the surface (diamond to star symbol), and experiences a second stage of vapor bubble growth during syn-eruptive quenching (star to circle symbol). (b) The blue melt inclusion follows an end-member PT path representative of an inclusion hosted within a low-Fo olivine. It experiences no cooling and post-entrapment crystallization at high temperature. A bubble only begins to grow during ascent to the surface, with 90% of the total bubble volume of this inclusion occurs during syn-eruptive quenching (star to circle). At the quenching rates of 10°C/s used in this model, there is negligible CO_2 transfer from the glass to the bubble during this low temperature phase of bubble growth. The large amount of bubble expansion without concurrent CO_2 diffusion causes the density of CO_2 in the vapor bubble to drop close to the detection limit of Raman spectroscopy (green line, d), while the CO_2 of the glass phase remains unchanged (c).

cooling rates, there is negligible transfer of CO_2 from the melt to the bubble during syn-eruptive quenching. Two end-member cooling histories were modeled. The red melt inclusion in Figure 9a experienced large amounts of cooling ($\Delta T = 150$°C) and PEC at high magmatic temperatures and pressures, representative of the PT path followed by melt inclusions hosted within the most forsteritic olivines. The blue melt inclusion in Figure 9b experiences no cooling and PEC prior to ascent and syn-eruptive quenching, representative of low-Fo melt inclusions which formed in carrier melts with similar temperatures to the melts in which they were erupted.

The high-Fo melt inclusion (red) grows a considerable proportion of its final bubble volume (58%) during PEC at high magmatic temperatures (square to star symbol; Figure 9a). The diffusion of CO_2 into this growing bubble causes the CO_2 content of the melt phase to drop rapidly (Figure 9c). During syn-eruptive quenching, there is no further CO_2 diffusion between the melt and bubble (Figure 9c). This stage of bubble growth accounts for 42% of the final volume, with ρ_{CO_2} decreasing from 0.10 to 0.06 g/cm^3 (Figures 9a and 9d). As the EOS method effectively predicts the density of CO_2 in the vapor bubble prior to the final, quench-induced stage of bubble expansion, the EOS method overpredicts the CO_2 density by a factor of 1.7× in this example. This lies well within the deviation between measured and predicted CO_2 contents for high-Fo F8 melt inclusions which have experienced >10% PEC (red line on Figure 8c). In reality, the proportion of the bubble grown at high temperatures will be substantially greater, as the model of Maclennan (2017) does not account for the FeO-loss process, which greatly increases the amount of PEC for a given ΔT. The volume of the bubble grown during syn-eruptive quench is determined by the difference between the temperature at the initiation of syn-eruptive quenching, and the glass transition temperature, so is almost constant for different PT paths. In contrast, with increasing amounts of PEC, the volume of the bubble grown at high temperatures gets progressively larger, so the relative expansion of the bubble during quench (and therefore the change in CO_2 density) gets progressively smaller. For example, in models with $\Delta T = 200$°C instead of $\Delta T = 150$°C, the amount of PEC increases from 18% to 25%, and the volume proportion of the bubble grown at high temperature increases from 58% to 68%. In turn, the bubble density drops from only

0.073 to 0.052 g/cm^3 during syn-eruptive quenching (so the EOS method would only over predict by a factor of ~1.4×).

In contrast, the low-Fo melt inclusion (blue) grows a very small proportion of its total bubble volume at high temperatures (10%), with 90% of the final bubble volume growing upon quench (Figure 9b). Substantial bubble expansion upon quench without concurrent CO_2 diffusion causes ρ_{CO_2} to drop substantially (Figure 9d). Effectively, the EOS method calculates the density of the bubble at the initiation of the quench stage (ρ_{CO_2} = 0.205 g/cm^3; star symbol), while the true bubble density is 11.9× lower (ρ_{CO_2} = 0.021 g/cm^3; circle symbol), close to the detection limit of Raman spectroscopy. This calculated discrepancy is very similar to that for vapor bubbles in low-Fo inclusions which do not have FDs (assuming the detection limit = 0.02 g/cm^3, cyan line, Figure 8c).

In summary, the EOS substantially overestimates ρ_{CO_2} for melt inclusions which have experienced small amounts of PEC and retain high CO_2 contents (Figures 8b and 8c), because bubble growth in these melt inclusions is dominated by the quenching process where there is no diffusion of CO_2 into the bubble. In contrast to these very large discrepancies (factors of ~10), bubble densities in melt inclusions which have experienced extensive PEC are broadly matched by the EOS method (within a factor of ~2; Figure 8c).

These bubble-growth models show that the magnitude of the discrepancy between measured bubble densities and those predicted by the EOS relates to the proportion of the bubble grown during syn-eruptive quenching. In contrast, Tucker et al. (2019) suggest that Raman measurements may underestimate ρ_{CO_2} relative to EOS methods because of the sequestration of significant quantities of CO_2 as thin films of solid carbonate on bubble walls. Carbonate phases have been identified in a number of melt inclusion vapor bubbles from subduction zone settings based on the presence of a distinctive peak in the Raman spectra at ~1,090 cm^{-1} (Moore et al., 2015; Venugopal et al., 2020). However, while Moore et al. (2015) report relatively abundant carbonate phases in vapor bubbles from Seguam and Fuego, only four of the 142 Kīlauean vapor bubbles they examined contained carbonates, all of which were hosted within a single olivine crystal. This suggests that vapor bubble carbonates are significantly less common in H_2O-poor ocean island systems. We observe no carbonate peaks in Raman spectra from F8 bubbles, nor during optical observations made prior to the exposure of bubbles during polishing. Additionally, no carbonate phases were identified during detailed examination of exposed bubble walls using backscatter and secondary electron imaging, and energy-dispersive spectroscopy (EDS) maps on a FEG-SEM. These EDS maps reveal that bubble wall coatings with a "dotted" appearance identified by Tucker et al. (2019) (see their Figure 2F) consist of Fe-Cu sulfides, rather than carbonates (see also Moore et al., 2015; Venugopal et al., 2020; Wieser, Jenner et al., 2020). Finally, even if carbonates in bubble walls remained undetected, our observations regarding the systematic relationship between PEC amounts, CO_2 contents, and the discrepancy between Raman measurements and the EOS would necessitate that only bubbles hosted in melt inclusions which had undergone negligible PEC contain carbonate phases.

5.5. Reconstructing Magma Storage Depths

Under the assumption that any reservoir from which a substantial proportion of the crystal cargo was derived must also have supplied melt (in order to entrain these crystals, and carry them to the surface), the depths of the main magma reservoirs supplying F8 can be estimated from melt inclusion entrapment pressures (for known crustal densities). Entrapment pressures were calculated from PEC-corrected total CO_2 and major element contents, and temperatures calculated using the MgO-liquid thermometer of Helz and Thornber (1987) for PEC-corrected MgO contents. As melt inclusion H_2O contents have been reset by diffusive re-equilibration, saturation pressures were calculated assuming H_2O = 0.5 wt%, based on the distribution of measured H_2O contents in literature studies of Kīlauean melt inclusions and undegassed submarine glasses from the ERZ (Figure 5b; Clague et al., 1995; Dixon et al., 1991; Sides, Edmonds, Maclennan, Houghton et al., 2014; Sides, Edmonds, Maclennan, Swanson et al., 2014; Tucker et al., 2019). Entrapment pressures for measured water contents are also shown in the Supporting Information. Entrapment pressures were converted into magma storage depths assuming ρ = 2,400 kg/m^3 (for consistency with modeling of the geodetic signals from the 2018 summit collapse by Anderson et al. (2019). Initially, we consider melt inclusions with no vapor bubble, or a vapor bubble which produced a FD, due to the uncertainty in the CO_2 density of vapor bubbles which do not contain a FD.

Literature studies of Kīlauean melt inclusions have mostly calculated saturation pressures using the CO_2-H_2O solubility model of Dixon et al. (1995) and Dixon (1997), implemented in the excel workbook VolatileCalc (Newman & Lowenstern, 2002, e.g., Moore et al., 2015; Sides, Edmonds, Maclennan, Houghton et al., 2014; Sides, Edmonds, Maclennan, Swanson et al., 2014; Tucker et al., 2019; Tuohy et al., 2016). VolatileCalc-Basalt uses a simplified relationship for the compositional dependence of CO_2 solubility expressed in terms of just the melt SiO_2 content, rather than the full compositional parameter Π which accounts for the abundance of seven cations (Dixon, 1997; Figure 6c). In this simplification the parameter $X_{CO_3^{2-}}(P_0,T_0)$, which represents the mole fraction of the carbonate ion in equilibrium with a specified fluid CO_2 fugacity at 1,200°C and 1 bar in the thermodynamic expression of Dixon et al. (1995), is expressed as:

$$X_{CO_3^{2-}}\left(P_0,T_0\right) = 8.7\times10^{-6} - 1.7\times10^{-7}\left[SiO_2\right]^{wt\%} \quad (6)$$

This relationship derives from the excellent linear correlation between Π and SiO_2 in a suite of lavas with 40–49 wt% from the North Arch Volcanic field (blue regression line; Figure 6c; Dixon et al., 1997). However, extrapolation of Equation 6 beyond 51.2 wt% SiO_2 returns a negative value for $X_{CO_3^{2-}}(P_0,T_0)$, which, in turn, predicts that the solubility of CO_2 is negative at all pressures. To avoid these extrapolation issues, VolatileCalc-Basalt does not let users enter a SiO_2 content >49 wt%, so most studies simply calculate the CO_2 solubility for melts with >49 wt% SiO_2 using the expression for SiO_2 = 49 wt% (e.g., Sides, Edmonds, Maclennan, Houghton et al., 2014; Sides, Edmonds, Maclennan, Swanson et al., 2014; Tucker et al., 2019). Newman and Lowenstern (2002) suggest that this approximation should return accurate entrapment pressures for basaltic compositions with up to 52 wt% SiO_2 contents. However, the simplified compositional parameter used in VolatileCalc-Basalt is only valid for melt compositions which define the same trajectories in Π versus SiO_2 space as the North Arch Lavas. F8 melt inclusions which have undergone >10% PEC are offset to substantially higher Π values at a given SiO_2 (Figure 6c), so VolatileCalc-Basalt underestimates the solubility of CO_2. In addition, while F8 melt inclusions show a large drop in Π with increasing SiO_2, all but four melt inclusions have SiO_2 > 49 wt%, so are treated as if they had the same composition in VolatileCalc-Basalt (red line; Figure 6c). Thus, VolatileCalc-Basalt not only underestimates CO_2 solubility, and therefore overestimates entrapment pressures for F8 melt inclusions hosted in high-Fo olivines, it also neglects compositional variations in CO_2 solubility within this suite (Figure 6c).

To demonstrate the importance of evaluating the suitability of different solubility models, we compare entrapment pressures from VolatileCalc-Basalt with the models of Ghiorso and Gualda (2015), hereafter MagmaSat, Iacono-Marziano et al. (2012) with hydrous coefficients, hereafter IM-2012, and Shishkina et al. (2014), hereafter S-2014, using the open-source python tool VESIcal (Iacovino et al., 2020). These three models utilize more than a decade of additional experiments on basaltic compositions compared to the expressions implemented in VolatileCalc-Basalt. By extension, these models are calibrated on a significantly larger compositional range (Figure 6a), so more effectively encapsulate variability in CO_2 solubility as a function of melt composition.

Entrapment pressures for melt inclusions hosted in low-Fo olivines from F8 calculated using VolatileCalc-Basalt, S-2014, and IM-2012 are statistically indistinguishable using the KS test at $p = 0.05$ (Figure 10a), likely because the major element compositions of these melt inclusions lie within the calibration range of all four solubility models (Figure 6a). MagmaSat returns slightly lower pressures, although these are not statistically distinguishable ($p = 0.1$ vs. S-2014). These slight discrepancies likely reflect the differential treatment of mixing between H_2O and CO_2 fluids in these different models (e.g., nonideal mixing in MagmaSat and IM-2012 vs. ideal mixing in S-2014 and VolatileCalc-Basalt; see Supporting Information Figure S1). As only two low-Fo melt inclusions have vapor bubbles producing a FD ($N = 2$), the distribution of entrapment pressures calculated using just glass CO_2 contents are indistinguishable from those using total CO_2 contents (dotted magenta vs. solid red lines; Figure 10a).

In contrast, there are substantial differences between the entrapment pressures obtained from different solubility models for high-Fo melt inclusions (>$Fo_{81.5}$), with MagmaSat and S-2014 plotting to significantly lower pressures than IM-2012 and VolatileCalc-Basalt (both pairs are statistically indistinguishable from one another at $p = 0.05$; Figure 10b). As discussed above, the simplification of the compositional dependence

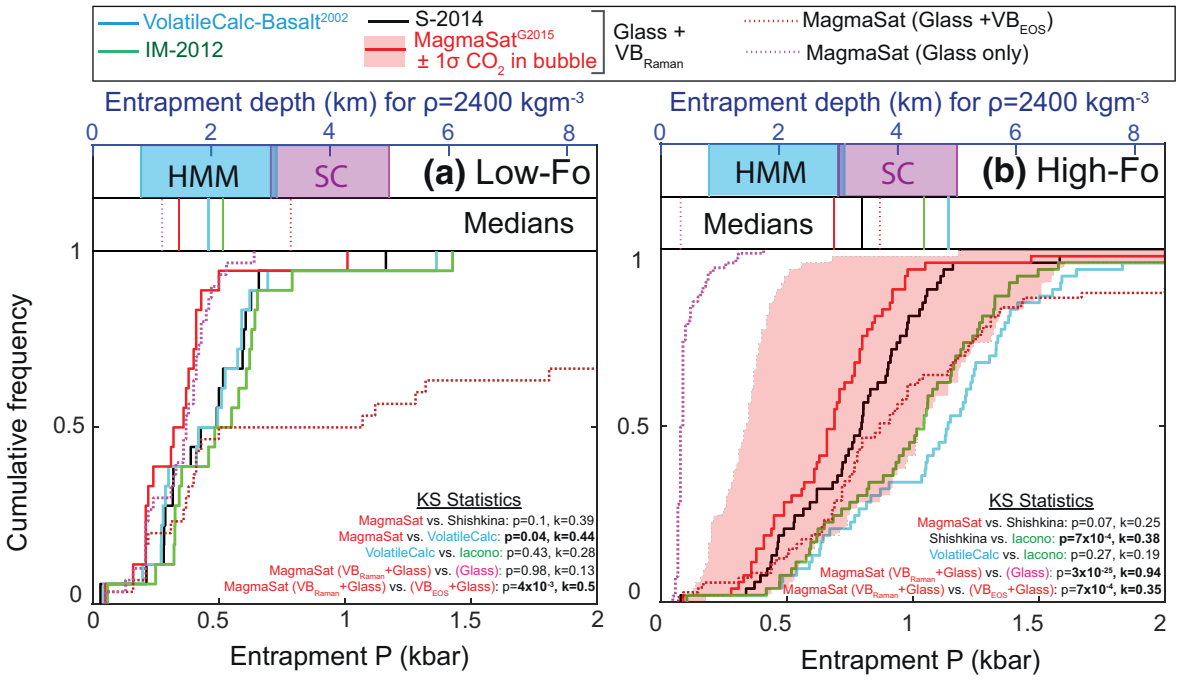

Figure 10. Cumulative distribution functions of entrapment pressures from different solubility models (major elements and CO_2 abundances corrected for the effects of PEC), with *p* values and test statistics from the KS test shown for different comparisons. (a) Entrapment pressures for melt inclusion hosted in low-Fo olivines (for melt inclusions with no VB, or a VB with a FD). Assuming ρ = 2,400 kg/m^3, the median depths for all solubility models align well with the depth range of the HMM reservoir from modeling of the first stage of the 2018 caldera collapse by Anderson et al. (2019) (upper and lower limits calculated from their median volume, centroid depth, and aspect ratio; cyan bar). The distributions of entrapment pressures from MagmaSat calculated from total carbon contents (bubbles + glass; red line) versus glass only measurements (pink dotted line) are statistically indistinguishable. Entrapment pressures from MagmaSat where bubble CO_2 contents are calculated using the EOS method lie to significantly higher pressures (deep red dotted line). (b) Entrapment pressures calculated for melt inclusions hosted in high-Fo olivines (for melt inclusions with a VB producing a FD). The light red region shows the error on MagmaSat entrapment pressures resulting from uncertainty in estimating bubble proportions from 2D images (Tucker et al., 2019). Entrapment depths considering this error window align well with geophysical estimates of the depth of the SC reservoir (3–5 km, magenta bar; Poland et al., 2015). Entrapment pressures from MagmaSat calculated using only glass CO_2 contents (dotted magenta line) are offset to very low pressures. Entrapment pressures calculated from bubble reconstructed using the EOS method are offset to anomalously high pressures. In (a) and (b), all melt inclusions are shown for glass-only measurements and EOS calculations, because studies which do not perform Raman measurements cannot distinguish between bubbles with and without a FD. EOS, equation of state; FD, Fermi diad; KS, Kolmogorov-Smirnov; PEC, post-entrapment crystallization.

in VolatileCalc-Basalt means that this model underestimates CO_2 solubility, and therefore overestimates entrapment pressures for high-Fo melt inclusions (Figure 6c). Similarly, Iacono-Marziano et al. (2012) warn that their semi-empirical model poorly incorporates the compositional effect of melt MgO contents on CO_2 solubility, as the vast majority of melts in their calibration data set have ~6–8 wt% MgO. In contrast, high-Fo PEC-corrected melt inclusions have MgO contents ranging from 7.8 to 13.7 wt% (Figure 6a). The calibration data set for the S-2014 model incorporates a significantly broader range of basaltic compositions, including melts with MgO contents similar to PEC-corrected high-Fo melt inclusions (Figure 6a). The MagmaSat calibration data set is similarly extensive (including the experiments used to calibrate S-2014, IM-2012, and VolatileCalc-Basalt). As for low-Fo melt inclusions, MagmaSat is offset to slightly lower pressures than S-2014 (median offset of 0.1 kbar).

Overall, we favor entrapment pressures from MagmaSat (Figure 11), as it has the largest calibration data set, and is a full thermodynamic model (whereas S-2014 is purely empirical). In addition, the S-2014 model is parameterized such that it predicts that ~1 wt% H_2O dissolves at 0 bar, meaning that saturation pressure calculations are effectively evaluating the solubility of pure CO_2 for the H_2O contents considered here (so saturation pressure does not change with variation in H_2O contents between 0 and 1 wt% H_2O, see Supporting Information Figure S1). As shown in Figure 10, differences between Shishkina and MagmaSat are relatively small. For high-Fo inclusions, the differences between these models are statistically insignificant, and easily overwhelmed with the errors associated with bubble volumes (error bars on Figure 11a). For completeness,

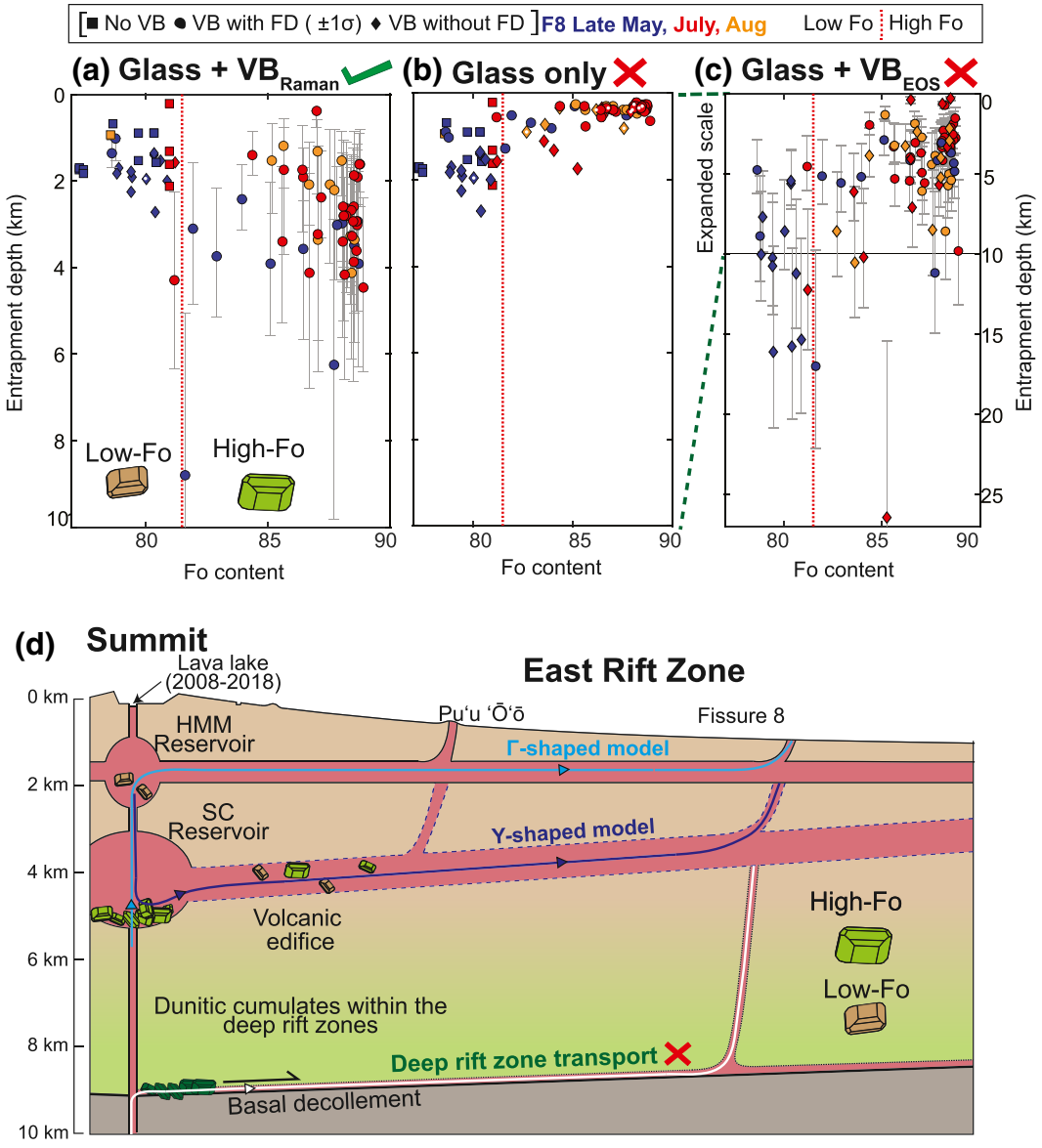

Figure 11. Schematic diagram of Kīlauea's plumbing system, informed by entrapment depths from MagmaSat for PEC-corrected melt inclusion compositions (assuming ρ = 2,400 kg/m^3 following Anderson et al. [2019]). (a) Preferred entrapment depths from this study (all melt inclusions for low-Fo olivines, only those with a FD for high-Fo olivines). Error bars on bubble-free melt inclusions from SIMS analyses are smaller than the symbol size. Error bars for bubble-bearing melt inclusions were calculated from the minimum and maximum possible total CO_2 content using the 1σ error calculated from repeated Raman analyses of each bubble, and the 1σ estimated by Tucker et al. (2019) associated with calculating 3D bubble volume proportions from 2D images (−48% to 37%). (b) Entrapment depths estimated from analyses of only the glass phase are anomalously shallow for high-Fo olivines. (c) Entrapment depths using the EOS method to reconstruct bubble CO_2 contents are anomalously deep, with large numbers of inclusions plotting at >5-km depth (note change in scale). Error bar reflects the uncertainty associated with calculating 3D bubble volume proportions from 2D images. (d) Cross-section showing the three hypothesized magma transport paths supplying rift zone eruptions. Depths are defined as the vertical distance beneath Kīlauea's summit. EOS, equation of state; FD, Fermi diad; PEC, post-entrapment crystallization; SIMS, secondary-ion mass spectrometry.

Supporting Information Figure S12 shows forsterite versus depth plots similar to those shown in Figure 11 for reconstructions using Shishkina, and for measured and fixed H_2O contents.

Using MagmaSat, low-Fo melt inclusions yield median entrapment depths (assuming ρ = 2,400 kg/m^3) of 1.44 km (lower and upper 68% = 0.89–1.74 km). The median centroid depth, aspect ratio and reservoir

volume derived from modeling of the first stage of the 2018 caldera collapse by Anderson et al. (2019) suggests that the HMM reservoir spans depths of 0.82–3.1 km. This depth range aligns well with our entrapment depths, which mainly cluster in the top half of that range (perhaps suggesting melt inclusion formation was favored in the upper half of the HMM reservoir). The low PEC amounts experienced by these melt inclusions, the absence of cracks, and the fact that the two low-Fo inclusions which did yield a diad had very low CO_2 densities (Figure 4c), suggests that melt inclusions with a vapor bubble which did not produce a FD likely contained very small quantities of CO_2 (because the bubble predominantly forming during syn-eruptive quench; Figure 9). Thus, we also consider entrapment depths from these melt inclusions (diamond shapes on Figure 11a). This extends the distribution of entrapment depths to slightly deeper depths, which show an even better overlap with the depths of the HMM reservoir suggested by Anderson et al. (2019).

Considering only high-Fo melt inclusions with a measurable FD (due to the uncertainty in the amount of CO_2 held within vapor bubbles which did not produce a FD in melt inclusions which have undergone extensive PEC), the distribution of entrapment depths (KS test, $p = 1.6 \times 10^{-7}$) and means (ANOVA, $p = 2.5 \times 10^{-6}$) are offset to significantly higher pressures than low-Fo melt inclusions (Figure 11a). Considering the error associated with reconstructing bubble CO_2 contents from bubble volumes estimated from 2D images (shown in pink on Figure 10b), the distribution of entrapment depths for high-Fo olivines overlaps remarkably well with geophysical estimates of the depth of the SC reservoir (3–5 km; Poland et al., 2015). In detail, entrapment depths for high-Fo olivines seem to form two main groups, one at ~2-km depth, and the second at 3–5-km depth (Figure 11a).

The quench-dominated mechanism of bubble growth in low-Fo olivines means that very little CO_2 is held within the vapor bubble. Thus, entrapment depths calculated using glass-only measurements are statistically indistinguishable from those combining bubble and glass measurements (Figure 10a). In contrast, entrapment depths calculated using just glass CO_2 contents in high-Fo olivines are anomalously shallow (median = 0.38 km, lower and upper 68% = 0.3–0.51 km; Figure 11b), because bubble growth at high temperatures during PEC has resulted in the vast majority of the CO_2 entering the vapor bubble (Figure 9).

Use of EOS techniques to reconstruct CO_2 contents of vapor bubbles yields very high entrapment depths for low-Fo olivines (median = 3.3 km, lower and upper 68% = 0.89–10.8 km; Figure 11c). Crucially, 13 inclusions yield entrapment depths >5 km (the inferred base of the SC reservoir), because the EOS method drastically overestimates bubble CO_2 densities in inclusions which have experienced minimal PEC (Figures 8b and 8c). For high-Fo olivines, there is a better overlap between entrapment depths calculated using EOS methods, and Raman measurements, and EOS methods get closer to the true distribution of entrapment pressures than measurements of only the glass phase (Figure 10b vs. c). However, EOS methods still predict that 23 melt inclusions crystallized at >5-km depth, with one forming at 26.4 km, compared to only two entrapment depths at 6.3 and 8.8 km using Raman reconstructions of bubble CO_2.

5.6. Summit-Rift Connectivity

Melt inclusion entrapment depths indicate that olivine crystals erupted at F8 crystallized within both the shallower HMM reservoir (low-Fo olivines) and the deeper, SC reservoir (high-Fo olivines, see also Lerner, 2020). The low degrees of olivine-melt disequilibrium and limited amounts of PEC experienced by melt inclusions hosted within low-Fo olivines implies that these crystals grew in a melt with a similar Mg#, and therefore temperature, to the carrier melt in which they were erupted. In contrast, the high degrees of olivine-melt disequilibrium and large amounts of PEC indicates that high-Fo crystals were mixed into a significantly lower Mg# (and therefore cooler) carrier liquid than the liquid in which they crystallized. Based on reports of lattice distortions (Gansecki et al., 2019) in some F8 olivines, high core forsterite contents, and the clustering of entrapment pressures between 3 and 5 km (Figure 11), we suggest that these olivines grew in the SC reservoir, and then settled into mush piles at the base of this reservoir where they were stored for prolonged periods (perhaps as long as centuries to millennia; Wieser, Edmonds et al., 2020).

Seismic swarms and the initiation of inflationary tilt in March–April 2018 have been interpreted to record the injection of new melts into the SC reservoir (Flinders et al., 2020; Neal et al., 2019), which may have disturbed the olivine mush pile. These new melts (along with the high-Fo olivines they scavenged) would then have mixed into the cooler, lower Mg# melts present within the middle to upper parts of the SC reservoir.

Alternatively, if inflationary signals were generated by a reduction in the amount of magma flowing along the ERZ to Pu‘u ’Ō’ō (Patrick et al., 2020), progressive internal pressurization of the SC reservoir could also disturb piles of settled crystals. Rapid cooling of mush-derived olivines following their mixing into more evolved melts would have initiated large amounts of PEC. Using the method of Danyushevsky et al. (2002, 2000), the degree of Mg# re-equilibration between melt inclusions and host olivine crystals (~70%–100%) indicates that crystals were resident in these cooler melts for timescales of approximately a month to a year prior to their eruption at F8. This is consistent with the time lag between geophysical signals indicating increasing pressurization of the magmatic system in March, and the eruption of crystals between late May and August.

The fact that only two melt inclusions record entrapment depths >5 km rules out models where high forsterite olivines grew in deeper magma storage reservoirs near the base of the volcanic pile (as suggested for Kīluaea’s prehistoric explosive period by Lynn et al., 2017), or within Kīlauea’s deep rift zones at ~6–9 km (Figure 11; Clague & Denlinger, 1994).

The mechanism by which crystal populations grown in the HMM and SC reservoirs were mixed into a single carrier melt encapsulates an ongoing debate at Kīlauea regarding the geometry of the connection between the rift zone conduit and the summit reservoir system. This connection has been variably described as a Y-shaped feeder system with the SC reservoir feeding both the HMM reservoir and the ERZ with two discrete conduits (Pietruszka et al., 2018; Poland et al., 2015, Model 2, Figure 11d), or a Γ-shaped feeder system with a vertical conduit between the HMM and the SC reservoir, and a single, near-horizontal conduit from the HMM reservoir into the ERZ (Cervelli & Miklius, 2003, Model 3, Figure 11d). Cervelli and Miklius (2003) suggest that the Γ-shaped model is more plausible because a shallow conduit (which is subject to less lithostatic pressure) is more likely to remain open during pauses in eruptive activity than a deep conduit, and because shallow intrusions into the upper ERZ influence both the HMM reservoir and activity at Pu‘u ’Ō’ō. However, Poland et al. (2015) favor the Y-shaped model based on earthquake and InSAR observations that dyke intrusions into the ERZ in 2007 and 2011 ascended from a depth of ~2–3 km.

For both reservoir geometries, the olivine mush pile at the base of the SC reservoir may have been disturbed by the input of new magma into Kīlauea’s summit inferred from geophysical signals (Flinders et al., 2020; Neal et al., 2019), or progressive internal pressurization due to a drop in magma output to Pu‘u ’Ō’ō. In the Γ-shaped model, high-Fo crystals sourced from the SC mush pile may have ascended into the HMM reservoir, and then been transported along a shallow rift zone conduit to the site of the eruption along with low-Fo olivines. However, the Y-shaped model provides an additional mechanism by which to disturb the SC mush pile. In this geometry, melts from the HMM reservoir carrying low-Fo olivine crystals would have drained down through the SC reservoir before passing out onto the rift zone, with significant potential for this downward flow, aided by the large scale collapse of Kīlauea’s caldera, to erode the SC mush pile. Interestingly, the proportion of crystals which are out of equilibrium with their carrier melts increases substantially between May–August 2018 (Figure 2a), and the degree of re-equilibration between melt inclusions and host crystals decreases (Figure 3b).

If the disturbance to the mush pile was solely the result of pressurization of the volcanic plumbing system, it might be expected that the majority of high-Fo olivines were disturbed from their mush piles in mid-March to April 2019, when inflationary signals were the strongest (Neal et al., 2019; Patrick et al., 2020). In this scenario, high-Fo olivines might be expected to be more dominant in the May 2018 versus July and August 2018 samples. In contrast, increasing erosion and scavenging of high-Fo olivines during the downdraining of melts from the HMM reservoir into the SC reservoir during the summit collapse could account for the increase in the proportion of high-Fo olivines with time, similar to the mechanism suggested by Teasdale et al. (2005) for the 1998 eruption of Cerro Azul, Galápagos. Erosion of the mush pile by downdraining from the shallower HMM reservoir, into which the summit caldera was collapsing, also accounts for the fact that high-Fo olivines were extremely rare during the 35 year Pu‘u ’Ō’ō eruption.

Another possibility is that some melt inclusions were trapped during the 40 km of transport down the ERZ to the site of the eruption (Patrick, Dietterich et al., 2019). Assessment of this hypothesis requires assumptions regarding the depth of magma transport. Given that the dyke to the LERZ propagated downrift from Pu‘u ’Ō’ō, we assume that the dyke had a similar depth to intrusions within the proximity of Pu‘u

ʻŌʻō between 1997 and 2007, which have been studied in detail, and shown to rise from the ERZ conduit at depths of ~2–2.4 km (Montgomery-Brown et al., 2011; Owen et al., 2000, and references within). Thus, it is plausible that some of the low-Fo olivines with entrapment depths near ~2 km may have growth in the rift zone. However, crystallization within the ERZ conduit and dyke would likely occur throughout the eruption, yet the abundance of low-Fo olivine crystals declined as the eruption proceeds.

The cluster of high-Fo olivines at ~2 km could also represent crystallization during downrift transport. These olivine crystals have Fo contents between 84 and 89, which must have grown from melts with MgO contents between 8.5 and 13.1 wt% (for $K_D = 0.3$, $FeO_T = 11.33$ wt%, with $Fe^{3+}/Fe_T = 0.15$). Yet, the highest erupted glass MgO content during the 2018 LERZ eruption is 6.74 wt% MgO (Figures 3a; Gansecki et al., 2019). Moreover, glass MgO contents during the 35-year Puʻu ʻŌʻō eruption did not exceed 8 wt% MgO (see Figure 8.2 of Thornber et al., 2015), suggesting that high MgO melts may not have been present in the rift zone conduit since the early phases of the Mauna Ulu eruption in 1969 (Wieser et al., 2019). In contrast, based on the occurrence of high MgO glass shards in a number of eruptions around the summit caldera, Helz et al. (2015) suggest that melts with 6.5–11 wt% MgO are present in the summit reservoir over many centuries. This observation supports our inference that the high-Fo olivines erupted at F8 crystallized from high MgO melts supplied from the Hawaiian mantle plume within the SC reservoir. These high MgO melts are very rarely erupted at the surface as they rapidly mix with more evolved, resident melts within the reservoir, so the only record of their existence are the olivines they crystallize. Given the rarity of these high MgO melts at the surface, it is difficult to imagine a situation where these melts would avoid mixing with resident magmas in the summit reservoir, and manage to travel prolonged distances along the ERZ conduit (which must be dominated by low MgO melts based on the composition of the co-erupted carrier liquid at F8). Finally, if these high-Fo olivines crystallized in the rift zone, they must have been resident for between a month and a year before they erupted at F8 (based on the degree of Mg# re-equilibration between melt inclusions and host olivine crystals).

Interestingly, the May 2018 sample does not show the distinctive clustering of high-Fo entrapment depths at ~2 km seen in the July and August 2018 sample. This may result from the relatively small number of measurements of high-Fo olivines in this sample ($N = 12$). Alternatively, it may suggest that the two reservoirs became increasingly connected during the collapse of the summit caldera, allowing remobilized high-Fo crystals from the SC mush pile to be transported up into the shallower HMM reservoir. The juxtaposition of these hot crystals with cooler melts within this reservoir may have led to dissolution or rapid growth (Mourey et al., 2020; Shea et al., 2019), favoring the formation of embayments. Perhaps due to the mixing with a hotter, and higher Mg# melt, growth may have resumed, sealing off melt inclusions recording shallower entrapment depths, before the crystal cargo was drained back down in the SC reservoir, and out along the ERZ conduit. It is also possible that the two reservoir systems always have a higher degree of connectivity than indicated by schematic diagrams such as Figure 11, with frequent cycling of melt and crystals between the two reservoirs (and it is simply chance that these lower pressure inclusions were not seen in the May 2018 sample). Further investigation of geophysical data sets from the 2018 eruption should provide tighter constraints on the depth of rift zone transport and dike propagation, allowing more rigorous assessments of the magma transport geometries indicated by our barometric estimates. In addition, more detailed work on timescales from diffusive re-equilibration of Fe-Mg in both melt inclusions and host crystals will help evaluate differences between the High-Fo crystal cargo erupted at F8 between May and August.

6. Conclusion

Detailed investigation of melt inclusion volatile systematics from the 2018 eruption of Kīlauea reveal that the erupted crystal cargo originated from both the Halemaʻumaʻu reservoir (low-Fo olivines; ~1–2-km depth) and the South Caldera reservoir (high-Fo olivines, ~3–5-km depth). Our work demonstrates that, in addition to the supply of magma from the HMM reservoir inferred from geophysical modeling of the summit collapse (Anderson et al., 2019), a substantial volume of magma must also have been derived from the SC reservoir in order to transport these high-Fo crystals to the surface. This interpretation is consistent with recent estimates of the total amount of SO_2 emitted from F8 (Kern et al., 2020), which requires the erupted volume to have been approximately twice that inferred to have drained from the HMM reservoir by Anderson et al. (2019).

High-Fo melt inclusions, which mostly yield entrapment depths that are aligned with geophysical estimates of the depth of the SC reservoir (~3–5 km), host the vast majority of their CO_2 budget in the vapor bubble (~90%). This is a consequence of the large amounts of PEC experienced by these melt inclusions following their entrainment into cooler, lower Mg# melts. Based on the textural and chemical similarities of these High-Fo crystals and those observed at previous eruptions at Kīlauea (Wieser et al., 2019; Wieser, Edmonds et al., 2020), we suggest that these olivines grew from high MgO melts present at the base of the SC reservoir (Helz et al., 2015), and settled into mush piles for prolonged time periods. Based on the degree of Mg# re-equilibration between melt inclusions and host olivines, we suggest that these olivines were mobilized from mush piles and mixed into lower Mg# carrier melts approximately a month to a year before they erupted at F8. This disturbance may correspond with the onset of geophysical signals of inflation in March–April 2018, interpreted to represent the injection of new melts into the plumbing system (Flinders et al., 2020), or a reduction in output from the summit reservoir (Patrick et al., 2020). Because of the large amount of CO_2 in the vapor bubbles of these inclusions, entrapment depths calculated using only glass CO_2 contents would yield anomalously low entrapment depths (~0.3–0.5 km), and fail to recognize that the SC reservoir supplied significant volumes of magma to F8.

In contrast, low-Fo melt inclusions are closer to equilibrium with their carrier melts, so have experienced smaller amounts of PEC. Where present, the vapor bubble in these melt inclusions is very CO_2-poor, and grew most of its volume during syn-eruptive quenching (~90%). As the quench rates of these samples mean that there was almost no diffusion of CO_2 between the melt and bubble during this growth phase, reconstructions of bubble CO_2 contents using EOS methods yield anomalously high entrapment depths (4.5–16.1 km; Figure 11c).

Careful choice of a CO_2-H_2O solubility model is also vital to obtain accurate entrapment pressures, and therefore depths. Importantly, the basaltic functions of VolatileCalc, which has been used by the majority of previous Kīlauean melt inclusion studies, overpredict entrapment pressures for high-Fo melt inclusions, due to the simplified relationship between CO_2 solubility and melt composition in this model. Like EOS methods, use of this model would indicate that ~50% of melt inclusions crystallized deeper than the base of the SC reservoir at >5 km (requiring the presence of a previously unrecognized storage reservoir; Figure 10).

Overall, our study highlights the importance of measuring bubble densities using Raman spectroscopy in addition to measurements of the melt phase by SIMS or FTIR. We also emphasize the importance of carefully evaluating the compositional range of different solubility models relative to the melt composition of interest. The strong agreement between our entrapment depths and models of magma storage inferred from geophysical data acquired at Kīlauea shows that melt inclusion records are a powerful tool to accurately constrain the location of magma storage reservoirs supplying volcanic eruptions.

Acknowledgments
This work was funded through a NERC DTP studentship to PW (NE/L002507/1), a NERC Edinburgh Ion Microprobe Facility grant (IMF675/1118), a Cambridge University Leave to Work away grant, and a grant from the NERC Center for Observation and Modeling of Earthquakes, Volcanoes and Tectonics (COMET). The authors thank Iris Buisman for help collecting EPMA data, Cees-Jan de Hoog and John Craven at the Edinburgh Ion Microprobe Facility for their assistance collecting SIMS data, and Richard Taylor (Zeiss) for collecting the EDS maps shown in the Supporting Information. The authors thank Emily Mason, Emma Liu, and Dave Schneider for help collecting samples in the field. We are very grateful to Jonathon Tucker to helping us to reproduce the EOS calculations in his paper, and for helpful discussions about bubble walls. Finally, we thank Paul Wallace, Kendra Lynn, and one anonymous reviewer, along with Associate Editor Ken Rubin for their helpful comments that greatly improved the quality of this manuscript.

Data Availability Statement

The melt inclusion and glass compositions presented in this paper are provided as an excel spreadsheet. This data has been uploaded to the Cambridge University Repository https://doi.org/10.17863/CAM.60202, and is also available on Github https://github.com/PennyWieser/G3-2018-MI. This spreadsheet also contains the results of the bubble growth models shown in Figure 9.

References

Anderson, A. T. (1974). Evidence for a picritic, volatile-rich magma beneath Mt. Shasta, California. *Journal of Petrology*, *15*(2), 243–267.

Anderson, A. T. & Brown, G. G. (1993). CO_2 contents and formation pressures of some Kilauean melt inclusions. *American Mineralogist*, *78*(7–8), 794–803.

Anderson, K. R., Johanson, I. A., Patrick, M., Gu, M., Segall, P., Poland, M. P., et al. (2019). Magma reservoir failure and the onset of caldera collapse at Kīlauea Volcano in 2018. *Science*, *366*(6470), eaaz1822.

Antoshechkina, P. M., & Ghiorso, M. S. (2018). MELTS for MATLAB: A new educational and research tool for computational thermodynamics. *AGUFM*, *2018*, ED44B–23.

Aster, E. M., Wallace, P. J., Moore, L. R., Watkins, J., Gazel, E., & Bodnar, R. J. (2016). Reconstructing CO_2 concentrations in basaltic melt inclusions using Raman analysis of vapor bubbles. *Journal of Volcanology and Geothermal Research*, *323*, 148–162.

Baker, S., & Amelung, F. (2012). Top-down inflation and deflation at the summit of Kīlauea Volcano, Hawaii observed with InSAR. *Journal of Geophysical Research*, *117*(B12), 1–14.

Barth, A., Newcombe, M., Plank, T., Gonnermann, H., Hajimirza, S., Soto, G. J., et al. (2019). Magma decompression rate correlates with explosivity at basaltic volcanoes—Constraints from water diffusion in olivine. *Journal of Volcanology and Geothermal Research*, *387*, 106664.

Bell, I. H., Wronski, J., Quoilin, S., & Lemort, V. (2014). Pure and pseudo-pure fluid thermophysical property evaluation and the open-source thermophysical property library coolprop. *Industrial & Engineering Chemistry Research*, *53*(6), 2498–2508.

Bennett, E. N., Jenner, F. E., Millet, M.-A., Cashman, K. V., & Lissenberg, C. J. (2019). Deep roots for mid-ocean-ridge volcanoes revealed by plagioclase-hosted melt inclusions. *Nature*, *572*(7768), 235–239.

Cervelli, P. F., & Miklius, A. (2003). The shallow magmatic system of Kilauea Volcano. *US Geological Survey Professional Paper*, *1676*, 149–163.

Chakraborty, S. (2010). Diffusion coefficients in olivine, wadsleyite and ringwoodite. *Reviews in Mineralogy and Geochemistry*, *72*(1), 603–639.

Clague, D., & Denlinger, R. (1994). Role of olivine cumulates in destabilizing the flanks of Hawaiian volcanoes. *Bulletin of Volcanology*, *56*(6–7), 425–434.

Clague, D., Moore, J., Dixon, J., & Friesen, W. (1995). Petrology of submarine lavas from Kilauea's Puna Ridge, Hawaii. *Journal of Petrology*, *36*(2), 299–349.

Collins, S., Maclennan, J., Pyle, D., Barnes, S.-J., & Upton, B. (2012). Two phases of sulphide saturation in réunion magmas: Evidence from cumulates. *Earth and Planetary Science Letters*, *337*, 104–113.

Danyushevsky, L., Della-Pasqua, F., & Sokolov, S. (2000). Re-equilibration of melt inclusions trapped by magnesian olivine phenocrysts from subduction-related magmas: Petrological implications. *Contributions to Mineralogy and Petrology*, *138*(1), 68–83.

Danyushevsky, L., & Plechov, P. (2011). Petrolog3: Integrated software for modeling crystallization processes. *Geochemistry, Geophysics, Geosystems*, *12*(7), 1–32.

Danyushevsky, L., Sokolov, S., & Falloon, T. J. (2002). Melt inclusions in olivine phenocrysts: Using diffusive re-equilibration to determine the cooling history of a crystal, with implications for the origin of olivine-phyric volcanic rocks. *Journal of Petrology*, *43*(9), 1651–1671.

Dixon, J. E. (1997). Degassing of alkalic basalts. *American Mineralogist*, *82*(3–4), 368–378.

Dixon, J. E., Clague, D. A., & Stolper, E. M. (1991). Degassing history of water, sulfur, and carbon in submarine lavas from Kilauea Volcano, Hawaii. *The Journal of Geology*, *99*(3), 371–394.

Dixon, J. E., Clague, D. A., Wallace, P., & Poreda, R. (1997). Volatiles in alkalic basalts form the North Arch volcanic field, Hawaii: Extensive degassing of deep submarine-erupted alkalic series lavas. *Journal of Petrology*, *38*(7), 911–939.

Dixon, J. E., Stolper, E. M., & Holloway, J. R. (1995). An experimental study of water and carbon dioxide solubilities in mid-ocean ridge basaltic liquids. Part I: Calibration and solubility models. *Journal of Petrology*, *36*(6), 1607–1631.

Duan, Z., & Zhang, Z. (2006). Equation of state of the H_2O, CO_2, and H_2O–CO_2 systems up to 10 GPa and 2573.15 K: Molecular dynamics simulations with ab initio potential surface. *Geochimica et Cosmochimica Acta*, *70*(9), 2311–2324.

Eaton, J. P., & Murata, K. (1960). How volcanoes grow. *Science*, *132*(3432), 925–938.

Esposito, R., Bodnar, R., Danyushevsky, L., De Vivo, B., Fedele, L., Hunter, J., et al. (2011). Volatile evolution of magma associated with the Solchiaro eruption in the Phlegrean Volcanic District (Italy). *Journal of Petrology*, *52*(12), 2431–2460.

Esposito, R., Klebesz, R., Bartoli, O., Klyukin, Y., Moncada, D., Doherty, A., & Bodnar, R. (2012). Application of the Linkam TS1400XY heating stage to melt inclusion studies. *Open Geosciences*, *4*(2), 208–218.

Fermi, E. (1931). Über den ramaneffekt des kohlendioxyds. *Zeitschrift für Physik*, *71*, 250–259.

Fiske, R. S., & Kinoshita, W. T. (1969). Inflation of Kilauea Volcano prior to its 1967-1968 eruption. *Science*, *165*(3891), 341–349.

Flinders, A., Caudron, C., Johanson, I., Taira, T., Shiro, B., & Haney, M. (2020). Seismic velocity variations associated with the 2018 lower East Rift Zone eruption of Kīlauea, Hawaii. *Bulletin of Volcanology*, *82*, 47.

Gaetani, G. A., O'Leary, J. A., Shimizu, N., Bucholz, C. E., & Newville, M. (2012). Rapid reequilibration of H_2O and oxygen fugacity in olivine-hosted melt inclusions. *Geology*, *40*(10), 915–918.

Gansecki, C., Lee, R. L., Shea, T., Lundblad, S. P., Hon, K., & Parcheta, C. (2019). The tangled tale of Kīlauea's 2018 eruption as told by geochemical monitoring. *Science*, *366*(6470), 1–9.

Gerlach, T., McGee, K., Elias, T., Sutton, A., & Doukas, M. (2002). Carbon dioxide emission rate of Kīlauea Volcano: Implications for primary magma and the summit reservoir. *Journal of Geophysical Research*, *107*(B9), ECV3–ECV315.

Ghiorso, M. S., & Gualda, G. A. (2015). An H_2O–CO_2 mixed fluid saturation model compatible with rhyolite-melts. *Contributions to Mineralogy and Petrology*, *169*(6), 1–30.

Giordano, D., Nichols, A. R., & Dingwell, D. B. (2005). Glass transition temperatures of natural hydrous melts: A relationship with shear viscosity and implications for the welding process. *Journal of Volcanology and Geothermal Research*, *142*(1–2), 105–118.

Gualda, G., Ghiorso, M. S., Lemons, R. V., & Carey, T. L. (2012). Rhyolite-MELTS: A modified calibration of MELTS optimized for silica-rich, fluid-bearing magmatic systems. *Journal of Petrology*, *53*, 875–890.

Hartley, M. E., Maclennan, J., Edmonds, M., & Thordarson, T. (2014). Reconstructing the deep CO_2 degassing behaviour of large basaltic fissure eruptions. *Earth and Planetary Science Letters*, *393*, 120–131.

Hartley, M. E., Neave, D. A., Maclennan, J., Edmonds, M., & Thordarson, T. (2015). Diffusive over-hydration of olivine-hosted melt inclusions. *Earth and Planetary Science Letters*, *425*, 168–178.

Hauri, E. (2002). SIMS analysis of volatiles in silicate glasses, 2: Isotopes and abundances in Hawaiian melt inclusions. *Chemical Geology*, *183*(1–4), 115–141.

Helo, C., Longpré, M.-A., Shimizu, N., Clague, D. A., & Stix, J. (2011). Explosive eruptions at mid-ocean ridges driven by CO_2-rich magmas. *Nature Geoscience*, *4*(4), 260–263.

Helz, R., Clague, D., Mastin, L. G., & Rose, T. R. (2015). Evidence for large compositional ranges in coeval melts erupted from Kīlauea's Summit Reservoir. *Hawaiian Volcanoes: From Source to Surface*, 125–145.

Helz, R., Clague, D. A., Sisson, T. W., & Thornber, C. R. (2014). Petrologic insights into basaltic volcanism at historically active Hawaiian volcanoes. *US Geological Survey Professional Paper*, *1801*, 237–292.

Helz, R., Cottrell, E., Brounce, M. N., & Kelley, K. A. (2017). Olivine-melt relationships and syneruptive redox variations in the 1959 eruption of Kīlauea Volcano as revealed by XANES. *Journal of Volcanology and Geothermal Research*, *333*, 1–14.

Helz, R., & Thornber, C. R. (1987). Geothermometry of Kilauea Iki lava lake, Hawaii. *Bulletin of Volcanology*, *49*(5), 651–668.

Iacono-Marziano, G., Morizet, Y., Le Trong, E., & Gaillard, F. (2012). New experimental data and semi-empirical parameterization of H_2O–CO_2 solubility in mafic melts. *Geochimica et Cosmochimica Acta*, *97*, 1–23.

Iacovino, K., Matthews, S., Wieser, P. E., Moore, G. M., & Begue, F. (2020). VESIcal Part I: An open-source thermodynamic model engine for mixed volatile (H2O-CO2) solubility in silicate melts. *EarthArxiv*, 1–58. https://eartharxiv.org/repository/view/1873/

Iacovino, K., & Till, C. B. (2019). Densityx: A program for calculating the densities of magmatic liquids up to 1,627°C and 30 kbar. *Volcanica*, *2*(1), 1–10.
Jarosewich, E. (2002). Smithsonian microbeam standards. *Journal of Research of the National Institute of Standards and Technology*, *107*(6), 681.
Kauahikaua, J. P., & Trusdell, F. A. (2020). Have humans influenced volcanic activity on the lower East Rift Zone of Kīlauea Volcano? A publication review (*Tech. Rep.). HVO: US Geological Survey.*
Kawakami, Y., Yamamoto, J., & Kagi, H. (2003). Micro-Raman densimeter for CO_2 inclusions in mantle-derived minerals. *Applied Spectroscopy*, *57*(11), 1333–1339.
Kern, C., Lerner, A. H., Elias, T., Nadeau, P. A., Holland, L., Kelly, P. J., et al. (2020). Quantifying gas emissions associated with the 2018 rift eruption of Kīlauea Volcano using ground-based DOAS measurements. *Bulletin of Volcanology*, *82*(7), 1–24.
Lamadrid, H., Moore, L., Moncada, D., Rimstidt, J., Burruss, R., & Bodnar, R. (2017). Reassessment of the Raman CO_2 densimeter. *Chemical Geology*, *450*, 210–222.
Lerner, A. (2020). *The depths and locations of magma reservoirs and their conse1428 quences for the behavior of sulfur and volcanic degassing*, PhD Thesis, University of Oregon. https://search.proquest.com/docview/2457313919?pq-origsite=gscholar&fromopenview=true
Lerner, A., Wallace, P. J., Shea, T., Mourey, A., Kelly, P., Nadeau, P., et al. (2020). Magma source depths and magma recycling in the 2018 eruption of Kīlauea, Hawai'i based on volatiles in melt inclusions. *AGU Fall Meeting Abstracts, 2020*, https://agu.confex.com/agu/fm20/meetingapp.cgi/Paper/669981
Le Voyer, M., Asimow, P. D., Mosenfelder, J. L., Guan, Y., Wallace, P. J., Schiano, P., et al. (2014). Zonation of H_2O and f concentrations around melt inclusions in olivines. *Journal of Petrology*, *55*(4), 685–707.
Lee, R. L., Wagoner, L., Conrey, R., Gansecki, C., & Lundblad, S. (2019). *Whole-rock chemical analyses of lava samples collected during the 2018 lower East Rift Zone eruption of Kilauea. U.S. Geological Survey*. Retrieved from https://www.sciencebase.gov/catalog/item/5d3279d2e4b01d82ce8791b2; https://doi.org/10.5066/P9LVY7GV
Lynn, K. J., Garcia, M., Shea, T., Costa, F., & Swanson, D. A. (2017). Timescales of mixing and storage for Keanakāko 'i Tephra magmas (1500–1820 CE), Kīlauea Volcano, Hawai'i. *Contributions to Mineralogy and Petrology*, *172*(9), 76.
Maaløe, S., Pedersen, R. B., & James, D. (1988). Delayed fractionation of basaltic lavas. *Contributions to Mineralogy and Petrology*, *98*(4), 401–407.
Maclennan, J. (2017). Bubble formation and decrepitation control the CO_2 content of olivine-hosted melt inclusions. *Geochemistry, Geophysics, Geosystems*, *18*(2), 597–616.
Matzen, A. K., Baker, M. B., Beckett, J. R., & Stolper, E. M. (2011). Fe–Mg partitioning between olivine and high-magnesian melts and the nature of Hawaiian parental liquids. *Journal of Petrology*, *52*(7–8), 1243–1263.
Montgomery-Brown, E. K., Sinnett, D., Larson, K., Poland, M. P., Segall, P., & Miklius, A. (2011). Spatiotemporal evolution of dike opening and décollement slip at Kīlauea Volcano, Hawai'i. *Journal of Geophysical Research*, *116*(B3), 1–14.
Moore, L. R., Gazel, E., Tuohy, R., Lloyd, A. S., Esposito, R., Steele-MacInnis, M., et al. (2015). Bubbles matter: An assessment of the contribution of vapor bubbles to melt inclusion volatile budgets. *American Mineralogist*, *100*(4), 806–823.
Moore, L. R., Mironov, N., Portnyagin, M., Gazel, E., & Bodnar, R. J. (2018). Volatile contents of primitive bubble-bearing melt inclusions from Klyuchevskoy volcano, Kamchatka: Comparison of volatile contents determined by mass-balance versus experimental homogenization. *Journal of Volcanology and Geothermal Research*, *358*, 124–131.
Moussallam, Y., Edmonds, M., Scaillet, B., Peters, N., Gennaro, E., Sides, I., & Oppenheimer, C. (2016). The impact of degassing on the oxidation state of basaltic magmas: A case study of Kīlauea Volcano. *Earth and Planetary Science Letters*, *450*, 317–325.
Moussallam, Y., Oppenheimer, C., Scaillet, B., Gaillard, F., Kyle, P., Peters, N., et al. (2014). Tracking the changing oxidation state of Erebus magmas, from mantle to surface, driven by magma ascent and degassing. *Earth and Planetary Science Letters*, *393*, 200–209.
Mourey, A., Shea, T., Costa, F., Shiro, B., Oalmann, J., Lee, R. L., & Gansecki, C. (2020). Preservation of Mantle-Derived Recharge Signatures in Olivine during Protracted Magma Storage. *Goldschmidt Abstracts 2020*, https://goldschmidt.info/2020/abstracts/abstractView?id=2020003748
Neal, C., Brantley, S., Antolik, L., Babb, J., Burgess, M., Calles, K., et al. (2019). The 2018 rift eruption and summit collapse of Kīlauea Volcano. *Science*, *363*(6425), 367–374.
Neave, D. A., Hartley, M. E., Maclennan, J., Edmonds, M., & Thordarson, T. (2017). Volatile and light lithophile elements in high-anorthite plagioclase-hosted melt inclusions from Iceland. *Geochimica et Cosmochimica Acta*, *205*, 100–118.
Neave, D. A., Maclennan, J., Edmonds, M., & Thordarson, T. (2014). Melt mixing causes negative correlation of trace element enrichment and CO_2 content prior to an Icelandic eruption. *Earth and Planetary Science Letters*, *400*, 272–283. https://doi.org/10.1016/j.epsl.2014.05.050
Newman, S., & Lowenstern, J. B. (2002). VolatileCalc: A silicate melt–H_2O–CO_2 solution model written in visual basic for excel. *Computers & Geosciences*, *28*(5), 597–604.
Owen, S., Segall, P., Lisowski, M., Miklius, A., Murray, M., Bevis, M., & Foster, J. (2000). January 30, 1997 eruptive event on Kilauea Volcano, Hawaii, as monitored by continuous GPS. *Geophysical Research Letters*, *27*(17), 2757–2760.
Pamukcu, A. S., Gualda, G. A., & Rivers, M. L. (2013). Quantitative 3D petrography using X-ray tomography 4: Assessing glass inclusion textures with propagation phase-contrast tomography. *Geosphere*, *9*(6), 1704–1713.
Patrick, M., Dietterich, H., Lyons, J., Diefenbach, A., Parcheta, C., Anderson, K. R., et al. (2019). Cyclic lava effusion during the 2018 eruption of Kīlauea Volcano. *Science*, *366*(6470), 1–10.
Patrick, M., Houghton, B., Anderson, K., Poland, M., Montgomery-Brown, E., Johanson, I., et al. (2020). The cascading origin of the 2018 Kīlauea eruption and implications for future forecasting. *Nature Communications*, *5646*, 1–13.
Patrick, M., Orr, T., Anderson, & Swanson, D. (2019). Eruptions in sync: Improved constraints on Kīlauea Volcano's hydraulic connection. *Earth and Planetary Science Letters*, *507*, 50–61.
Pietruszka, A. J., Marske, J. P., Heaton, D. E., Garcia, M. O., & Rhodes, J. M. (2018). An isotopic perspective into the magmatic evolution and architecture of the rift zones of Kīlauea Volcano. *Journal of Petrology*, *59*(12), 2311–2352.
Poland, M. P., Miklius, A., & Montgomery-Brown, E. K. (2015). Magma supply, storage, and transport at shield-stage Hawaiian volcanoes. *US Geological Survey Professional Paper*, *1801*, 179–234.
Rasmussen, D., Plank, T., Wallace, P., Newcombe, M., & Lowenstern, J. (2020). Vapor-bubble growth in olivine-hosted melt inclusions. *American Mineralogist*, *105*(12), 1898–1919. https://doi.org/10.2138/am-2020-7377
Riker, J. (2005). *The 1859 eruption of Mauna Loa Volcano, Hawai'i: Controls on the development of long lava channels (Unpublished doctoral dissertation)*. University of Oregon.
Roedder, E. (1979). Origin and significance of magmatic inclusions. *Bulletin de Mineralogie*, *102*(5), 487–510.

Roedder, E. (1984). Fluid inclusions. Reviews in Mineralogy: Mineralogical Society of American, Vol. 12.
Roeder, P., & Emslie, R. (1970). Olivine-liquid equilibrium. *Contributions to Mineralogy and Petrology*, *29*(4), 275–289.
Rosso, K., & Bodnar, R. (1995). Microthermometric and Raman spectroscopic detection limits of CO_2 in fluid inclusions and the Raman spectroscopic characterization of CO_2. *Geochimica et Cosmochimica Acta*, *59*(19), 3961–3975.
Ruth, D. C., Costa, F., de Maisonneuve, C. B., Franco, L., Cortés, J. A., & Calder, E. S. (2018). Crystal and melt inclusion timescales reveal the evolution of magma migration before eruption. *Nature Communications*, *9*(1), 2657.
Ryan, M. P., & Sammis, C. G. (1981). The glass transition in basalt. *Journal of Geophysical Research: Solid Earth*, *86*(B10), 9519–9535.
Schneider, C. A., Rasband, W. S., & Eliceiri, K. W. (2012). NIH image to ImageJ: 25 years of image analysis. *Nature Methods*, *9*(7), 671–675.
Shea, T., Hammer, J. E., Hellebrand, E., Mourey, A. J., Costa, F., First, E. C., et al. (2019). Phosphorus and aluminum zoning in olivine: Contrasting behavior of two nominally incompatible trace elements. *Contributions to Mineralogy and Petrology*, *174*(10), 85.
Shishkina, T., Botcharnikov, R. E., Holtz, F., Almeev, R. R., Jazwa, A. M., & Jakubiak, A. A. (2014). Compositional and pressure effects on the solubility of H_2O and CO_2 in mafic melts. *Chemical Geology*, *388*, 112–129.
Shishkina, T., Botcharnikov, R., Holtz, F., Almeev, R., & Portnyagin, M. V. (2010). Solubility of H_2O-and CO_2-bearing fluids in tholeiitic basalts at pressures up to 500 MPa. *Chemical Geology*, *277*(1–2), 115–125.
Sides, I., Edmonds, M., Maclennan, J., Houghton, B. F., Swanson, D., & Steele-MacInnis, M. J. (2014). Magma mixing and high fountaining during the 1959 Kīlauea Iki eruption, Hawai'i. *Earth and Planetary Science Letters*, *400*, 102–112.
Sides, I., Edmonds, M., Maclennan, J., Swanson, D., & Houghton, B. (2014). Eruption style at Kīlauea Volcano in Hawai'i linked to primary melt composition. *Nature Geoscience*, *7*(6), 464–469.
Skirius, C. M., Peterson, J. W., & Anderson. (1990). Homogenizing rhyolitic glass inclusions from the bishop tuff. *American Mineralogist*, *75*(11–12), 1381–1398.
Span, R., & Wagner, W. (1996). A new equation of state for carbon dioxide covering the fluid region from the triple-point temperature to 1100 K at pressures up to 800 MPa. *Journal of Physical and Chemical Reference Data*, *25*(6), 1509–1596.
Steele-Macinnis, M., Esposito, R., & Bodnar, R. J. (2011). Thermodynamic model for the effect of post-entrapment crystallization on the H_2O–CO_2 systematics of vapor-saturated, silicate melt inclusions. *Journal of Petrology*, *52*(12), 2461–2482.
Taracsák, Z., Hartley, M., Burgess, R., Edmonds, M., Iddon, F., & Longpré, M. (2019). High fluxes of deep volatiles from ocean island volcanoes: Insights from El Hierro, Canary Islands. *Geochimica et Cosmochimica Acta*, *258*, 19–36.
Teasdale, R., Geist, D., Kurz, M., & Harpp, K. (2005). 1998 Eruption at Volcán Cerro Azul, Galápagos Islands: I. Syn-eruptive petrogenesis. *Bulletin of Volcanology*, *67*(2), 170–185.
Thornber, C. R., Orr, T. R., Heliker, C., & Hoblitt, R. P. (2015). Petrologic testament to changes in shallow magma storage and transport during 30+ years of recharge and eruption at Kılauea Volcano, Hawai'i. *Hawaiian Volcanoes: From Source to Surface*, *208*, 147.
Tucker, J. M., Hauri, E. H., Pietruszka, A. J., Garcia, M. O., Marske, J. P., & Trusdell, F. A. (2019). A high carbon content of the Hawaiian mantle from olivine-hosted melt inclusions. *Geochimica et Cosmochimica Acta*, *254*, 156–172.
Tuohy, R. M., Wallace, P. J., Loewen, M. W., Swanson, D. A., & Kent, A. J. (2016). Magma transport and olivine crystallization depths in Kīlauea's East Rift Zone inferred from experimentally rehomogenized melt inclusions. *Geochimica et Cosmochimica Acta*, *185*, 232–250.
Venugopal, S., Schiavi, F., Moune, S., Bolfan-Casanova, N., Druitt, T., & Williams-Jones, G. (2020). Melt inclusion vapour bubbles: The hidden reservoir for major and volatile elements. *Scientific Reports*, *10*(1), 1–14.
Vinet, N., & Higgins, M. D. (2010). Magma solidification processes beneath Kilauea Volcano, Hawaii: A quantitative textural and geochemical study of the 1969–1974 Mauna Ulu Lavas. *Journal of Petrology*, *51*(6), 1297–1332.
Wallace, P. J., & Anderson. (1998). Effects of eruption and lava drainback on the H_2O contents of basaltic magmas at Kilauea Volcano. *Bulletin of Volcanology*, *59*(5), 327–344.
Wallace, P. J., Kamenetsky, V. S., & Cervantes, P. (2015). Special collection: Glasses, melts, and fluids, as tools for understanding volcanic processes and hazards. melt inclusion CO_2 contents, pressures of olivine crystallization, and the problem of shrinkage bubbles. *American Mineralogist*, *100*(4), 787–794.
Wang, W., Caumon, M.-C., Tarantola, A., Pironon, J., Lu, W., & Huang, Y. (2019). Raman spectroscopic densimeter for pure CO_2 and CO_2-H_2O-NaCl fluid systems over a wide pt range up to 360°C and 50 MPa. *Chemical Geology*, *528*, 119281.
Whitty, R. C., Ilyinskaya, E., Mason, E., Wieser, P. E., Liu, E. J., Schmidt, A., et al. (2020). Spatial and temporal variations in SO_2 and $PM_{2.5}$ levels around Kīlauea Volcano, Hawai'i during 2007–2018. *Frontiers of Earth Science*, *8*, 36.
Wieser, P. E., Edmonds, M., Maclennan, J., Jenner, F. E., & Kunz, B. E. (2019). Crystal scavenging from mush piles recorded by melt inclusions. *Nature Communications*, *10*(1), 1–11.
Wieser, P. E., Edmonds, M., Maclennan, J., & Wheeler, J. (2020). Microstructural constraints on magmatic mushes under Kīlauea Volcano, Hawai'i. *Nature Communications*, *11*(1), 1–14.
Wieser, P. E., Jenner, F., Edmonds, M., Maclennan, J., & Kunz, B. E. (2020). Chalcophile elements track the fate of sulfur at Kīlauea Volcano, Hawai'i. *Geochimica et Cosmochimica Acta*, *282*, 245–275. Retrieved from https://doi.org/10.1016/j.gca.2020.05.018
Wright, T. L., & Fiske, R. S. (1971). Origin of the differentiated and hybrid lavas of Kīlauea Volcano, Hawai'i. *Journal of Petrology*, *12*(1), 1–65.